OAK RIDGE
NATIONAL LABORATORY
MANAGED BY UT-BATTELLE
FOR THE DEPARTMENT OF ENERGY

ORNL/TM-2013/259
Approved for public release.

Final Report

Recovery Act - Development and application of processing and process control for nano-composite materials for lithium ion batteries

July 31, 2013

Prepared by

Claus Daniel, Beth Armstrong, Curt Maxey, Adrian Sabau, and Hsin Wang
Oak Ridge National Laboratory

Patrick Hagans and Susan Babinec
A123 Systems, Inc.

With contributions from other researchers

UT-BATTELLE
ORNL-27 (4-00)

ORNL/TM-2013/259

Department of Energy
Office of Energy Efficiency and Renewable Energy
Advanced Manufacturing Office

FINAL REPORT

Recovery Act - Development and application of processing and process control for nano-composite materials for lithium ion batteries

Claus Daniel, Beth Armstrong, Curt Maxey, Adrian Sabau, Hsin Wang
Patrick Hagans, Susan Babinec

DOE CPS Number: 18981
Project Period (12:09 – 06:13)

July 2013

Prepared by
OAK RIDGE NATIONAL LABORATORY
Oak Ridge, Tennessee 37831-6283
managed by
UT-BATTELLE, LLC
for the
U.S. DEPARTMENT OF ENERGY
under contract DE-AC05-00OR22725

and A123 Systems, Inc.
Ann Arbor, MI

CONTENTS

LIST OF FIGURES v
LIST OF TABLES ix
Acknowledgements 1
Acronyms 3
Executive Summary 5
1. Objective 7
2. Introduction 8
3. Benefits to the Funding DOE Office's Mission 9
4. Technical Discussion of Work Performed by All Parties 10
4.1 Process Charterization 10
4.1.1 Characterization of Optical and Thermophysical Properties 10
4.1.2 In-situ Measurement Of Temperatures And Infrared Heat Fluxes During The Processing Of Electrode Materials 10
4.2 Process modeling and simulation 21
4.2.1 Radiative Transport Model for Drying Using Infrared Heating 21
4.2.2 Mass transfer module for drying 26
4.2.3. Stress Model 40
4.3 Process Development 50
4.3.1 Coating Development 50
4.3.2 Critical Thickness Determination and Drying Study 53
4.3.3 Design evaluation of high speed web handling system 54
4.4 Development of Quality control and safety testing 56
4.4.1 Online Quality Control 56
4.4.2 Safety testing 58
5. Subject Inventions 66
5.1 In-situ drying evaluation 66
5.2 In-line quality control procedure 66
6. Commercialization Possibilities 68
7. Plans for Future Collaboration 68
8. Conclusions 70
9. References 72

LIST OF FIGURES

Figure 1. Measured emissivity. 10

Figure 2. Thermocouple placement on top surface of the foil: (a) center and (b) center and edge. 12

Figure 3. Temperature evolution for uncoated anode foils at a conveyor belt speed of 300 mm/min: (a) top and back surfaces of the foil – in the center of the foil, (b) on the back-side of the foil in the center and edge of the foil. 13

Figure 4. Temperature evolution for anode foils during the drying of the NCS coating at conveyor belt speeds of (a) 150 mm/min and (b) 350 mm/min. B and C indicate two different runs for each condition. 13

Figure 5. Temperature evolution for anode foils during the drying of the NCS coating at conveyor belt speeds of (a) 450 mm/min and (b) 600 mm/min. 14

Figure 6. Pictures showing the placement of the heating pad approximately (a) 1-1.5" inside the convection oven (default) and (b) 1" outside the convection oven (new). 14

Figure 7. Temperature evolution for cathode foils during the drying of the NCS coating at conveyor belt speeds of 350 mm/min for cases in which the heating pad was placed approximately (a) 1" inside the convection oven and (b) 1" outside the convection oven. 15

Figure 8. Temperature evolution for the cathode foils during the drying of the NCS coating at conveyor belt speeds of 350 mm/min for cases in which the heating pad was placed approximately 1" inside and outside the convection oven. 15

Figure 9. Temperature evolution for three positions of the IR bank for cathode foils during the drying of the NCS coating at conveyor belt speeds of 350 mm/min (a) entire duration and (b) detail for temperature ranges of 60 to 130 ^{o}C. 16

Figure 10. Temperature evolution for coated electrodes at 350 mm/min coating speed. 16

Figure 11. Temperature evolution for coated cathode (final coating thickness of 36 μm) at 900 mm/min coating speed. In the second experiment, an initial coating of twice the initial coating thick coating the coating was incomplete dried. 17

Figure 12. Temperature evolution for coated cathode (final coating thickness of 36 μm) at 400 mm/min coating speed. Excellent reproducibility shown by running three different experiments. 17

Figure 13. Temperature evolution for coated cathode (final coating thickness was not measured) at 800 mm/min coating speed. The two runs without NCS coating were shown together with the coating run. 18

Figure 14. IR lamp bank and electrode foil. 19

Figure 15. Locations (x,y) at which the heat flux was measured. 19

Figure 16. Variation of the heat flux along the electrode foil, i.e., x axis. 19

Figure 17. Variation of the heat flux with the power level of the IR system (right below the at the centerline of the front face of the IR fixture) 20

Figure 18. Spectrum of the incident radiation from the IR lamps: (a) wavelength [0:8] μm, and (b) zoom in on a wavelength domain [0.2:0.8] μm. 22

Figure 19. Index of refraction for the materials used in the NCS coating. 24

Figure 20. Extinction coefficient for NMP and PVDF (a) NMP- measured at ORNL, PVDF – materials data from Solef[R] brand, (b) NMP – FTIR data obtained from Shui et al. 2006, PVDF materials data from Kynar[R] brand. 24

Figure 21. Estimated optical properties for the NCS coating at different coating thicknesses during drying (initial coating thickness was 75 μm): (a) index of refraction, (b), extinction coefficient, and (d) penetration depth (thickness at which radiation intensity would be decreased by 1/e or 36.7%). . 25

Figure 22. Schematic showing the foil transition regions at the entrance to the oven and exit from the oven. Different temperatures of the oven walls are also shown. 27

Figure 23. Schematic of solid phase packing as the coating thickness decreases due to solvent evaporation. The third picture represents the coherency point, where the particles touch each other and the coating would be able to support some stress. 28

Figure 24. Typical data during drying: (a) raw micro-balance signal [g] and (b) estimated weight loss and (c) temperature variation and (d) temperature variation for both the top thermocouple and another thermocouple wrapped into one side of the Al foil. 33

Figure 25. Experimental and computed temperature results for the drying of a coating on an anode foil at 35 cm/min foil speed (β=1.0e-5). 34

Figure 26. Drying of a coating on an anode foil at 35 cm/min foil speed (β=5.0e-4): (a) experimental and computed temperatures; (b) fractions of solvent (L), solids (S), and air (a); and (c) coating thickness 35

Figure 27. Drying of a coating on an anode foil at 35 cm/min foil speed (β=1.5e-4): (a) experimental and computed temperatures; (b) fractions of solvent (L), solids (S), and air (a); and (c) coating thickness 36

Figure 28. Time dependence results for drying of a coating on an anode foil at 35 cm/min foil speed (β=1.5e-4): (a) computed fractions of solvent (L), solids (S), and air (a); and (b) computed coating thickness 36

Figure 29. Estimated average air temperature, $\mathbf{0.5}\boldsymbol{Tg} + \boldsymbol{Ts}$, used to evaluate properties for estimating natural convection effects. 37

Figure 30. Preliminary results for the mass transport coefficient for drying of the NCS coating using natural convection correlations. 37

Figure 31. *Time dependence* results for drying of a coating on an anode foil at 35 cm/min foil speed using evaporation rates based on mass transport coefficients: (a) computed fractions of solvent (L), solids (S), and air (a); and (b) computed coating thickness. 38

Figure 32. Young's modulus estimations using different formulations. 48

Figure 33. Young's modulus as a function of solid fraction in the coating. Upper line represents the data without any upper limit, i.e., just using the Maxwell averaging. Lower line represents the data that includes an upper limit for the Young's modulus. 48

Figure 34. 100X image comparing surfaces from slurries of different mixing times. 51

Figure 35. Slurry mixed at >40 minutes has excellent stability over three days. 51

Figure 36. Slurries of range of solids, up to 1.8X the original, were developed which have the appropriate target viscosities. 51

Figure 37. Appropriate gap positioning eliminates gas trapping/bubble formation, which can lead to cracks. Web thickness uniformity eliminates variations which can result in cracking. 52

Figure 38. A – initial cracking with optimized slurry and equipment results in cracking at high stress points – such as the edges, B – surface at 100X and optical surface profile showing that nonuniformities of +/- 1.2um were obtained once IR heating was implemented. 52

Figure 39. Micrographical series of dried coating with determination of on-set cracking and critical thickness 54

Figure 40. Thickness across the width of a coating. 54

Figure 41. High speed web handling system manufactured by Conquip, CA with full tension control, speed control, unwind and rewind. Treatment options can be added at several locations. 55

Figure 42. Initial experimental setup. 56

Figure 43. Solid-state power supply diagram. 57

Figure 44. Humidity control algorithm 58

Figure 45. Schematic of the ORNL pinch test 59

Figure 46. Displacement and Voltage vs. Time plot of a pinch test. 59

Figure 47. Concept of modified pinch test for cell components and the final setup. 60

Figure 48. Load and Voltage vs Time plots during a baseline separator test. 61

Figure 49. Separator areas with original porosity (left) and area under the compression (right). 61

Figure 50. Typical Metal-Separator-Metal sample with sharp voltage drop at failure point. 62

Figure 51. Typical Anode – separator – Cathode sample with sloped voltage drop prior to the failure point. 63

Figure 52. Anode – Ceramic coated separator – Cathode sample with sloped voltage drop prior to the failure point. 63

Figure 53. Close-up look at Anode – Ceramic coated separator – Cathode sample with sloped voltage drop prior to the failure point. 64

LIST OF TABLES

Table 1. Thermocouples considered 11

Table 2. The evolution of volumetric fraction of the solvent, g_{sol}, binder, g_{bin}, and solid particles, g_p, during drying of an initial slurry thickness of 75 μm and final coating thickness of 11 μm 22

Table 3. Total reflectivity, R, absorptivity in the coating, A[%] 26

Table 4. Data on the initial and final conditions of the coating 28

Table 5. Mass transport coefficients 30

Table 6. Properties of dry air for obtaining the temperature variation effects on natural convection (Bejan, 2004) 32

Table 7. Cases considered for the evaporation coefficient β 35

Table 8. Thermophysical properties 38

Table 9. Main features needed for the stress analysis during drying of coatings on flexible multiple layered substrates 43

Table 10. Yield strength [MPa] of PVDF at different temperatures and strain rates 46

Table 11. Properties of different constituent materials used in the analysis 47

Table 12. Slurry equipment parameters 50

ACKNOWLEDGEMENTS

The work described in this report under CRADA NFE-08-01826 has been funded by the Advanced Manufacturing Office through CPS agreement 18981 and A123 Systems, Inc. for the Office of Energy Efficiency and Renewable Energy as CPS project number 18981. The authors thank the rest of the R&D team, namely Hungoo Cho, Ralph Dinwiddie, William Hicks, Jane Howe, Jim Kiggans, Andrew Payzant, Shawn Reeves, and David Wood for their invaluable technical contributions making this project successful.

The authors are grateful for the local program support by Craig Blue, Alan Liby, Hiram Rogers, Angie Blankenship and the headquarters program support by the Advanced Manufacturing Office.

ACRONYMS

AMO	Advanced Manufacturing Office
CRADA	Cooperative Research and Development Agreement
DEMA	Differential Effective Medium Approximation
DOE	Department of Energy
FEA	Finite Element Analysis
FTIR	Fourier Transform Infrared Spectroscopy
HEV	Hybrid Electric Vehicle
IR	Infrared
NCS	Nanocomposite Separator
NMP	N-Methyl-2-pyrrolidone
ORNL	Oak Ridge National Laboratory
PBX	Polymer Bounded Explosives
PHEV	Plug-in Hybrid Electric Vehicle
PVDF	Polyvinylidene Fluoride
RTE	Radiation Transport Equations
TcB	Temperature center of Backside

EXECUTIVE SUMMARY

Oak Ridge National Laboratory and A123 Systems, Inc. collaborated on this project to develop a better understanding, quality control procedures, and safety testing for A123 System's nanocomposite separator (NCS) technology which is a cell based patented technology and separator. NCS demonstrated excellent performance. x3450 prismatic cells were shown to survive >8000 cycles (1C/2C rate) at room temperature with greater than 80% capacity retention with only NCS present as an alternative to conventional polyolefin. However, for a successful commercialization, the coating conditions required to provide consistent and reliable product had not been optimized and QC techniques for being able to remove defective material before incorporation into a cell had not been developed. The work outlined in this report addresses these latter two points.

First, experiments were conducted to understand temperature profiles during the different drying stages of the NCS coating when applied to both anode and cathode. One of the more interesting discoveries of this study was the observation of the large temperature decrease experienced by the wet coating between the end of the infrared (IR) drying stage and the beginning of the exposure to the convection drying oven. This is not a desirable situation as the temperature gradient could have a deleterious effect on coating quality. Based on this and other experimental data a radiative transfer model was developed for IR heating that also included a mass transfer module for drying. This will prove invaluable for battery coating optimization especially where IR drying is being employed.

A stress model was also developed that predicts that under certain drying conditions tensile stresses are formed in the coating which could lead to cracking that is sometimes observed after drying is complete. Prediction of under what conditions these stresses form is vital to improving coating quality.

In addition to understanding the drying process, other parameters such as slurry quality and equipment optimization were examined. Removal of particles and gels by filtering, control of viscosity by %solids and mixing adjustments, removal of trapped gas in the slurry and modification of coater speed and slot die gap were all found to be important for producing uniform and flaw-free coatings.

Second, an in-line Hi-Pot testing method has been developed specifically for NCS that will enable detection of coating flaws that could lead to soft or hard electrical shorts within the cell. In this way flawed material can be rejected before incorporation into the cell thus greatly reducing the amount of scrap that is generated.

Improved battery safety is an extremely important benefit of NCS. Evaluation of battery safety is usually accomplished by conducting a variety of tests including nail penetration, hot box, over charge, etc. For these tests entire batteries must be built but the resultant temperature and voltage responses reveal little about the breakdown mechanism. In this report is described a pinch test which is used to evaluate NCS quality at various stages including coated anode and cathode as well as assembled cell. Coupled with post-microscopic examination of the damaged 'pinch point' test data can assist in the coating optimization from an improved end-use standpoint.

As a result of this work two invention disclosures, one for optimizing drying methodology and the other for an in-line system for flaw detection, have been filed. In addition, two papers are being written for submission to peer-reviewed journals.

1. OBJECTIVE

In 2008, the United States experienced the highest gasoline prices in its history at almost $4/gallon and also experienced a continuously unstable supply of oil at high risk. As a result, sales of hybrid electric vehicles (HEV) increased and several automakers announced plans to develop plug-in hybrid electric vehicles (PHEV). However, sales of Japanese HEVs remained in the 2-3% range of all vehicles and U.S. auto manufacturers were struggling to introduce them. An important step for a continued effort to electrify the drive train and revolutionize the way to energy efficient mobility remains the development of cost effective, long lasting, and abuse tolerant Li-ion batteries.

A123 Systems Inc. is successfully providing safe and affordable Li-ion batteries for power tools and limited mile range HEV – PHEV conversion kits. A123 Systems Inc. is one of the leading battery developers in the United States enabling and revolutionizing energy efficient mobility. A newly developed nano-composite material with potential to significantly improve device performance has been developed by the company. Energy savings will occur from development of a successful manufacturing process, which enables applications including the transportation market.

However, in order to satisfy vehicle needs and bring the new material from the lab scale to market, there was a need to optimize the formulation of the nano-composite material and to scale up the manufacturing process while maintaining its nano-feature characteristics. Additionally, low cost processing and quality control measures needed to be developed for successful implementation of this material into a safe and reliable lithium ion battery cell.

Oak Ridge National Laboratory (ORNL) is the largest multi-disciplinary Department of Energy (DOE) research laboratory with extensive experience in materials science, ceramics and composites, processing science, and quality control. ORNL utilized A123 Systems Inc.'s proprietary material for the development of the needed low cost processing technology. New processing technology was developed including advanced deposition techniques which offer sub-micrometer thickness control and a drying and post treatment technology, all while controlling the microstructure at the nano-scale. ORNL provides unique facilities for ceramic processing, photonic processing, in-situ characterization and quality control.

2. INTRODUCTION

This project targeted the development of optimized processing, process control and quality measures for a homogenous and reliable deposition and treatment of a nano-composite coating to be used in lithium ion battery technology with guidelines for scale-up and mass production of the product. It developed a fundamental understanding of the nanomaterial behavior, the process mechanisms, and the resulting functionality. The project integrated a quality control approach with a science and technology to produce a reliable product and enable lithium ion battery technology for transportation and stationary applications.

The primary purpose of the effort was to advance the state of the nanomanufacturing of this nano-composite material for Li-ion batteries such that improvements in reliability in the material and in its production will be enabled, and the scale-up of the technology will become more economically feasible.

The intent was to enable the nanocomposite film technology in a commercially viable 63450 prismatic cell format and then to establish the understanding to guide a future pilot scale production using cell designs and processes amenable to high volume manufacturing. Both high and low power applications are envisioned for this technology, and so success was defined somewhat differently in each case. In both instances, the cost must be significantly less than traditional commercial polyolefin separators and the nanocomposite separator (NCS) should provide break-through high temperature stability, which means mechanical stability at 200°C.

For high power applications, cells having the technology will provide at least 30% improved power and maintain 80% capacity at > 1200 cycles (at high discharge rates) while cycling at room temperature, and >600 cycles at 60°C. For low power applications, cells having the technology must maintain 80% capacity at > 2000 cycles (at low discharge rates) while cycling at room temperature, and 800 cycles at 60°C.

The aim of the project was to utilize existing processing science, modeling, and quality control capabilities at ORNL to develop the current A123 nanocomposite film and develop improved coating technology and quality control measures. The focus was centered on characterization of the existing defects in the A123 separator and the development of an understanding of the defect formation mechanisms. A combined computational and process development effort led to the success of the new material and guide the pathway to a successful scale-up to mass production.

The nanotechnology of interest is a separator, which is hereafter called “NCS” for nanocomposite separator.

3. BENEFITS TO THE FUNDING DOE OFFICE'S MISSION

The work performed under this project directly supported DOE's mission in the Advanced Manufacturing Office of the Office of Energy Efficiency and Renewable Energy by developing a material system, and its processing conditions to be used in electrochemical energy storage systems for automotive and other industrial applications. Electrochemical energy storage systems help reduce the nation's energy intensity and reduce the nation's dependence on foreign oil as well as help reduce the emission of greenhouse gases. This project was in collaboration between Oak Ridge National Laboratory and A123 Systems, Inc. It focused on manufacturing of energy storage devices and addressed processing conditions, theoretical knowledge and modeling and simulation, and safety evaluation of the materials and systems.

4. TECHNICAL DISCUSSION OF WORK PERFORMED BY ALL PARTIES

4.1 PROCESS CHARTERIZATION

For a successful processing of NCS, a thorough process characterization is needed. First, material property data was needed as input to the computer simulations. Second, the process characterization and generated data was utilized for section 4.2 on modeling and simulation of experimental aspects in order to eliminate the cracking and pinhole defects that form during the drying process.

4.1.1 Characterization of Optical and Thermophysical Properties

Reflectivity and optical and other thermophysical properties had been measured to provide a base input for the subsequent modeling tasks. The reflectivity was measured using an integrated sphere apparatus. The reflectivity was measured for several electrode materials, both uncoated and coated with the nanocomposite coating. Since both the anode and cathode included the current collectors they are opaque. Thus the emissivity can be obtained simply, as E=1-R.

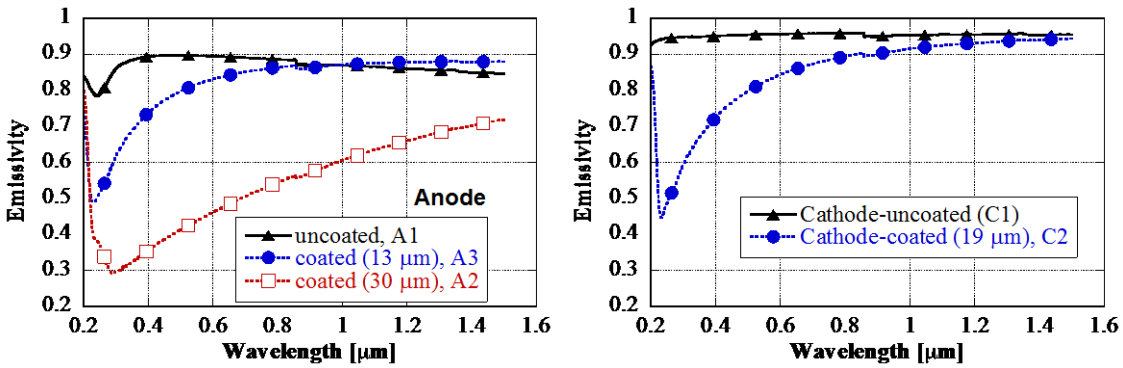

Figure 1. Measured emissivity.

The thermophysical properties include the specific heat, thermal conductivity, and density. A literature review was conducted to obtain thermophysical properties of various materials involved in the process. These properties are available for the materials that are used to make the electrodes and the amount of individual compounds in the electrodes can be used to estimate the properties of different electrodes using mixture laws (Maleki et al. 1999).

4.1.2 In-situ Measurement of Temperatures and Infrared Heat Fluxes During the Processing of Electrode Materials

A data acquisition system from ORNL was used to acquire data on electrode temperatures during electrode processing. The incident heat fluxes from the infrared (IR) lamp bank to the electrode surface were measured using a heat flux sensor. The temperature data were acquired at different locations on the electrode foil.

Experimental procedure for temperature measurements

Several thermocouple types were reviewed in order to assess their applicability to the A123 laboratory setup. Thermocouples and their fixtures have to fulfill several requirements:

(1) Wires must be insulated through an external sheath in order to minimize the heating effects of the wires away from the thermocouple junction and thus ensure that the thermocouple junction was at the appropriate temperature. For the actual laboratory setup, the heating effects that could induce artifacts in the data were due to the IR lamps and heating pad in the oven.
(2) The thermocouples must have a small time response in order to enable the acquisition of accurate data, as the thermal process is transient.
(3) The thermocouples beads must be placed on the electrode foil.
(4) The length of the wires, excluding the plastic connectors, must be long enough such that they can be used to acquire data during an entire pass of the electrode foil through the IR system and convection oven.

In order to fulfill the first condition, the fiberglass-insulated thermocouple wire leads were chosen. Thin and ultrathin thermocouple wires were chosen to have an appropriate time response. Several surface thermocouples were chosen and thermocouples were made out of very fine thermocouples wires.

Table 1. Thermocouples considered

Name	***Wire Size [mm(in)]***	***Response time [ms]***	***Feature***	***Applicability***	***Experimental use***
SA1XL-K		150	self-adhesive surface thermocouples	self-adherence would insure adequate contact	self-adherent glue worked only once
CO1-K	0.013 mm (0.0005")	10-20	flat junction	can handle curved surfaces	Very good experience
CO3-K	0.25 mm (0.01")	250*	wire thickness, beaded thermocouple	very good time response	Very good experience
GG-K-36	0.13 mm (0.005")	100*	glass braid insulation		Not used since TT-K-40 is better
TT-K-40	0.08 (0.003")	30*	neoflon PFA insulation		Very good experience

*estimated from data supplied by vendor for air

The surface thermocouples CO1-K and CO3-K and thermocouples made with the neoflon PFA insulation wires TT-K-40 were successfully used in the experiments. The surface thermocouples CO1-K were taped either on the top and back-side of the electrode foil. The surface thermocouples were used for most electrode foils that were uncoated. In order to assess the temperature variation across the width of the electrode, the thermocouples were also placed on the centerline of the foil and 1” away from the edge of the foil.

(a) 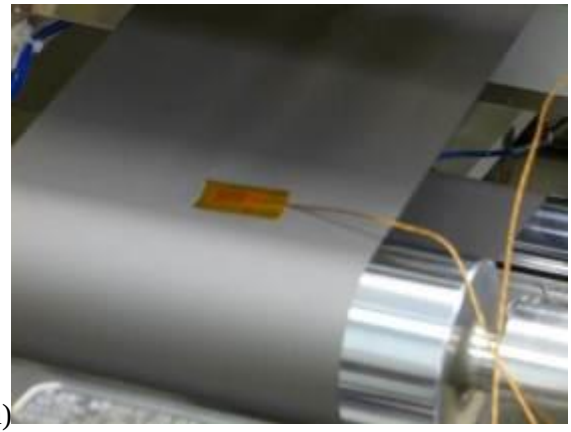 (b) 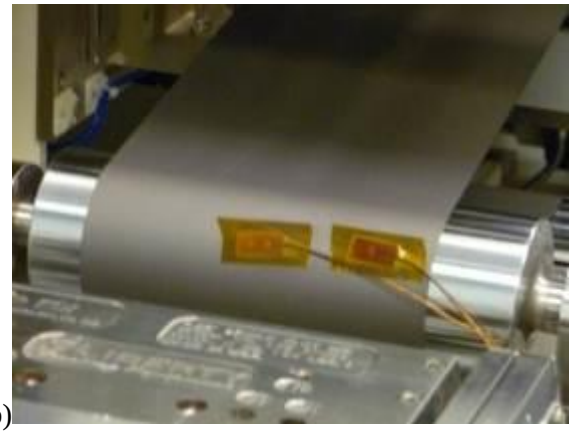

Figure 2. Thermocouple placement on top surface of the foil: (a) center and (b) center and edge.

Temperature measurements for uncoated anode foils

Experiments were conducted for the bare anode foils and bare cathode foils at different speeds of the conveyor belt, ranging from 150 mm/min up to 900 mm/min. In some cases, the foil was moved continuously while in other cases it was started after a holding period of time. Thus some variation was noted between cases that were run at the same speed, depending on the start-up time. For cases in which the foil was stopped and the temperature was measured right after the start-up, the electrode foil was heated more by the IR as it was held below the IR for a longer time than for the continuous runs.

In Figure 3, the temperature evolution is shown for uncoated anode foils at a conveyor belt speed of 300 mm/min. The results shown in Figure 2a indicate the following features:

1) The first bell-shape feature, at times of 60 to 110s, indicates the heating prior to reaching the first roll – the roll that was next to the slot-die machine and subsequent cooling due to the foil contact with the roll.
2) We have to mention that the coating would have been deposited at about 125 s in this case, right as the temperature started to rise abruptly.
3) The IR heating is indicated by the sharp temperature rise, from approximately 125s until 145 s.
4) Then a sharp temperature drop is recorded as the foil enters the furnace (145-200s).
5) The temperature rose again due to the heating pad in the furnace.
6) There were six humps in the temperature profile, each due to the contact of the foil with the small rolls in the oven.
7) The temperature drops sharply after it passed over the last two rolls.

The temperature on the centerline of the back side, TcB, shows lower temperatures as the foil passed above the IR system than the temperature on the centerline of the top side, TcT (Figure 3a). In the oven, TcB > TcT, which is expected as the heated pad is placed on the bottom of the oven. In Figure 3b, the temperature on the centerline of the back side, TcB, is shown with the temperature near the edge of the foil on the back side, TeB. As expected, TcB > TeB, with the highest temperature difference, TcB – TeB, of approximately 10 ^{o}C.

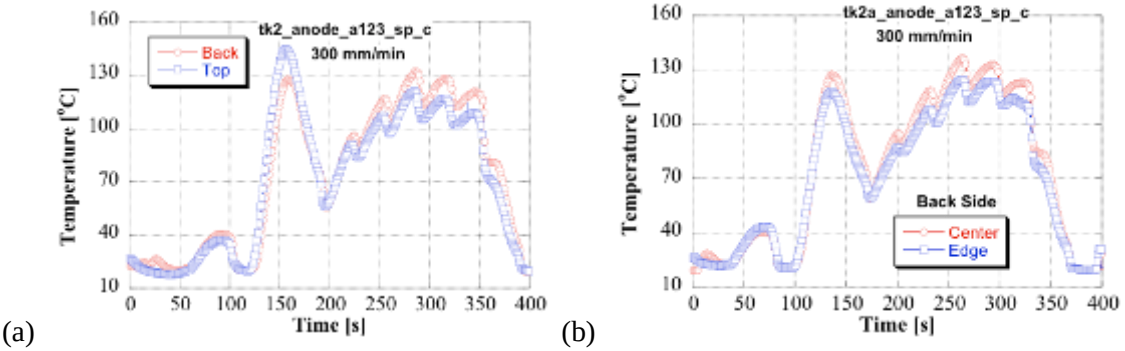

(a) (b)

Figure 3. Temperature evolution for uncoated anode foils at a conveyor belt speed of 300 mm/min: (a) top and back surfaces of the foil – in the center of the foil, (b) on the back-side of the foil in the center and edge of the foil.

The most intriguing feature of the temperature profile is the "V"-like evolution, which occurred at times between 145s and 200s as the foil enters the oven. The temperature drop is due to several factors including (1) the lack of IR heating as the light is obstructed by the oven entrance and (2) the low temperature of the heating pad at the entrance.

Temperature measurements for NCS coated anode foils

Since the clearance between the slot-die and the electrode foil was very small, in order to deposit a 200-300 mm film coating, it was not possible to use the surface thermocouples for the coated samples. For the coated samples, only the TT-K-40 thermocouples were used. In order not to disturb the coating, the thermocouples were taped on the back-side of the electrode foil, after the electrode foil exited the slot-die and the coating was deposited.

In Figure 4, the temperature evolution is shown for anode foils during the drying of the NCS coating. A very good coating was deposited during these runs. Two independent runs were conducted for each conveyor speed, showing excellent reproducibility of the measurements. In Figure 5, the temperature evolution is shown for both uncoated and coated anode foils. The results indicate that slightly higher temperatures were observed for the uncoated foils. The temperature difference was approximately 10°C. The lower temperature for the coated foils is expected as extra heat is needed to evaporate the solvent N-Methyl-2-pyrrolidone (NMP).

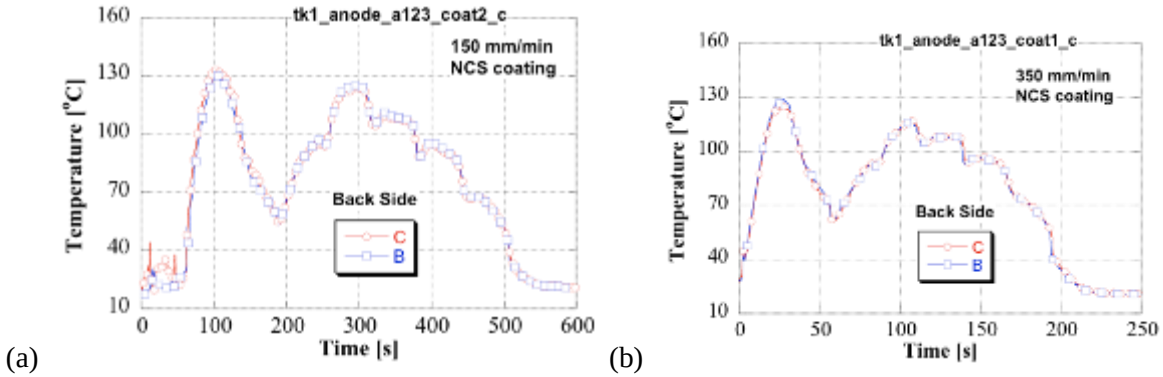

(a) (b)

Figure 4. Temperature evolution for anode foils during the drying of the NCS coating at conveyor belt speeds of (a) 150 mm/min and (b) 350 mm/min. B and C indicate two different runs for each condition.

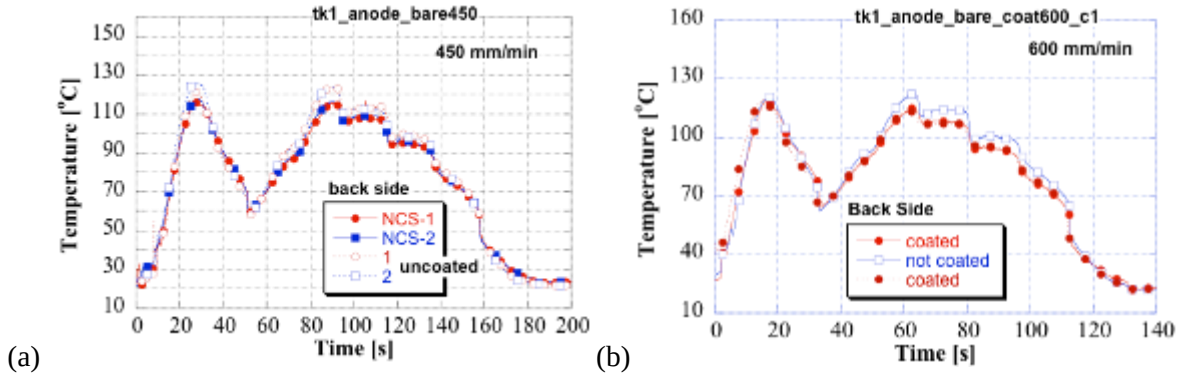

Figure 5. Temperature evolution for anode foils during the drying of the NCS coating at conveyor belt speeds of (a) 450 mm/min and (b) 600 mm/min.

Temperature measurements for coated cathode foils

Figure 6a shows a picture of the default arrangement of the heating pad. In order to decrease the temperature drop as the foil enters the oven, the heating pad was pulled outside the oven for approximately 1 inch in (Figure 6b). The temperatures for the default pad placement and the new heating pad position are shown in Figures 11a and 11b. The temperature drop was reduced by 13 ^{o}C by moving the heating pad. A direct comparison between the two results shown in Figure 7 is shown in Figure 8 (the data shown in Figure 7b was translated such that the IR heating would occur at similar times in both cases).

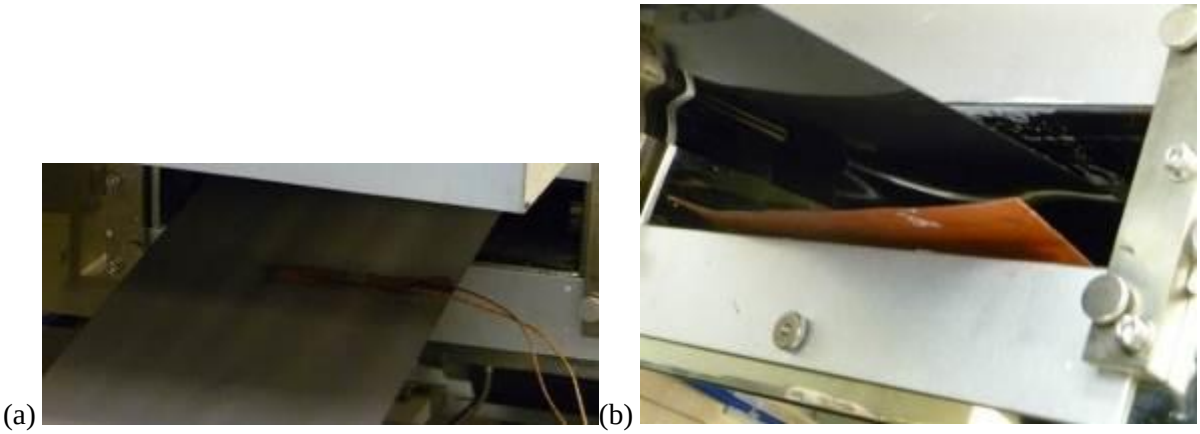

Figure 6. Pictures showing the placement of the heating pad approximately (a) 1-1.5" inside the convection oven (default) and (b) 1" outside the convection oven (new).

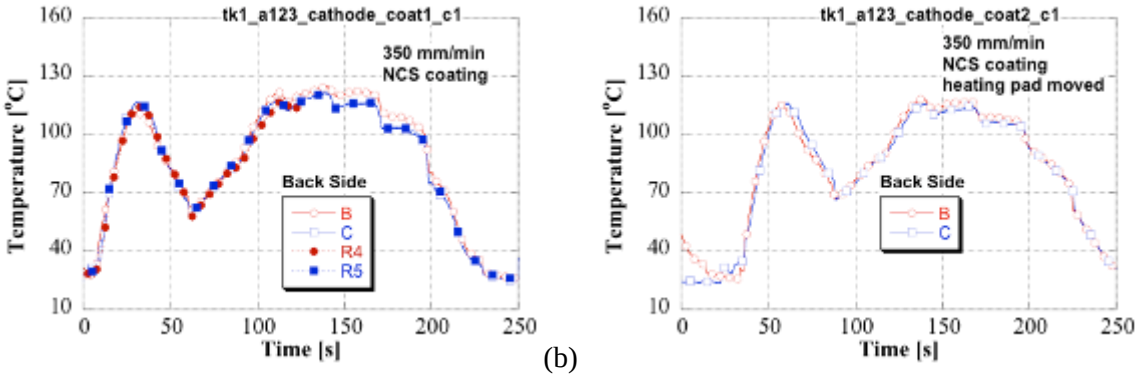

Figure 7. Temperature evolution for cathode foils during the drying of the NCS coating at conveyor belt speeds of 350 mm/min for cases in which the heating pad was placed approximately (a) 1" inside the convection oven and (b) 1" outside the convection oven.

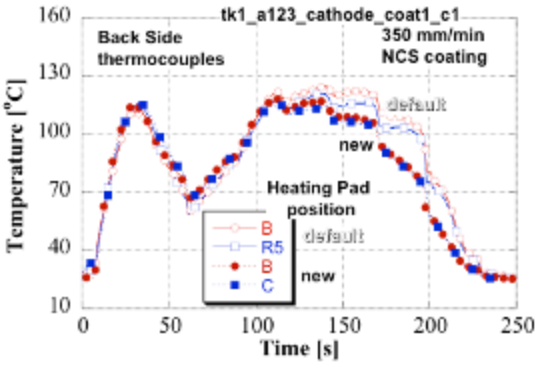

Figure 8. Temperature evolution for the cathode foils during the drying of the NCS coating at conveyor belt speeds of 350 mm/min for cases in which the heating pad was placed approximately 1" inside and outside the convection oven.

In order to assess the effect of the IR bank lamps on the temperature drop, which occur as the foil enters the oven, the IR fixture was moved closer to the convection oven. The measured temperatures for the default position (3.25 in away from the convection oven) and two other positions of the IR fixture are shown in Figure 9. The temperature results show that moving the IR fixture close to the convection oven results in higher peak temperatures during the IR heating phase while the temperature drop stays approximately the same.

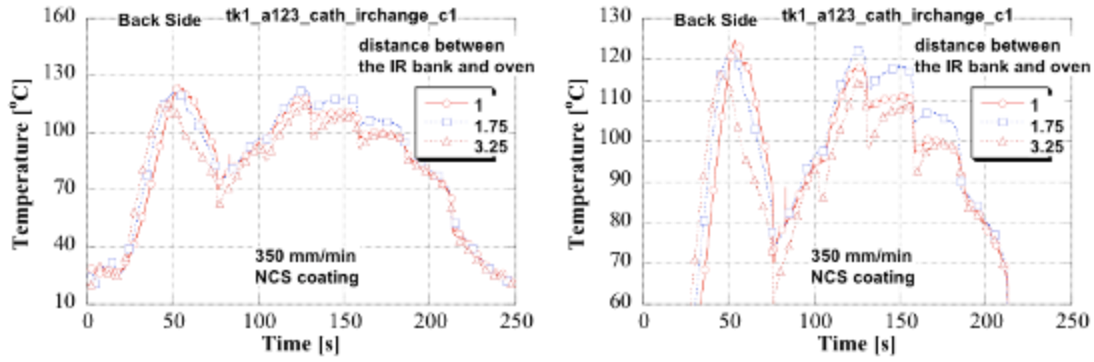

Figure 9. Temperature evolution for three positions of the IR bank for cathode foils during the drying of the NCS coating at conveyor belt speeds of 350 mm/min (a) entire duration and (b) detail for temperature ranges of 60 to 130 °C.

In Figure 10, a direct comparison is made between the temperatures measured during the NCS coating and drying of the anode and cathode. The results show that although the anode foil is heated to higher temperatures during the IR exposure, the anode foil reaches cooler temperatures in the convection oven.

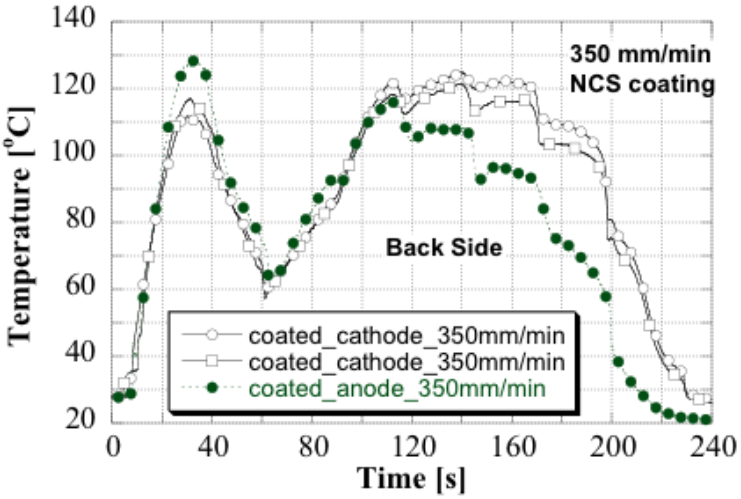

Figure 10. Temperature evolution for coated electrodes at 350 mm/min coating speed.

In the remainder of this section, the results are shown in Figures 15, 16, and 17 for the coating process when a second furnace was added to the first one. The second drying furnace used a floating web technique in which hot air was blown from elements above and below the web in order to keep the web floating, i.e., without using rolls within the furnace to suspend the web. Each "air-blowing" element that was used in the second furnace had two IR heating bulbs in its center section while the air was blown at the edges at each element. The highest speed web considered in these runs was 900 mm/min. In Figure 11, the drying of a 36 μm thick coating on a cathode was shown at a web speed of 900 mm/min. The spikes seen in the temperature variation indicate the effect of the IR heating within each air-blowing element in the second furnace. Although not shown here since temperature data was not recoded, we have to mention that a coating that was dried to a final thickness of 44 μm at the

same 900 mm/min web speed exhibited micro-cracks, which were visible under 20x microscope magnification. By decreasing the web speed to 400 mm/min, we can observe that the temperature of the web has also increased (Figure 12). The spikes seen in the temperature variation, which indicate the effect of the IR heating, are much more distinct now. The spikes with the higher temperature indicate the elements that are positioned below the web, while those with the lower temperature peaks indicate those that were positioned above the web. Finally, the web speed was lowered to 300 mm/min while thicker coatings were cast (Figure 13). We have to mention that large cracks were obvious, even without magnification, for the 85 μm thick coating, while no cracks were observed for the 45 μm thick coating. It is an open question how the temperature spikes in the second furnaces would affect the quality of the coating.

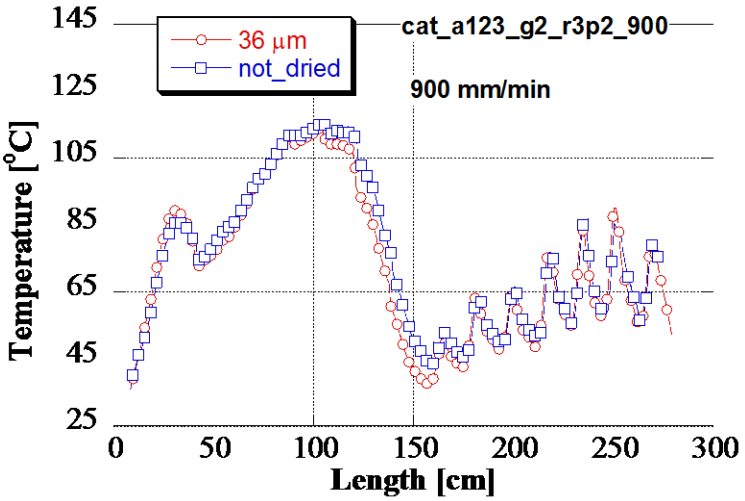

Figure 11. Temperature evolution for coated cathode (final coating thickness of 36 μm) at 900 mm/min coating speed. In the second experiment, an initial coating of twice the initial coating thick coating the coating was incomplete dried.

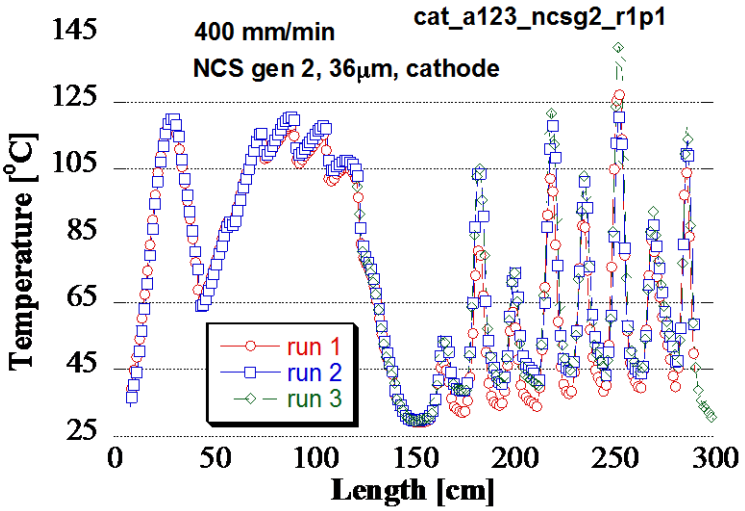

Figure 12. Temperature evolution for coated cathode (final coating thickness of 36 μm) at 400 mm/min coating speed. Excellent reproducibility shown by running three different experiments.

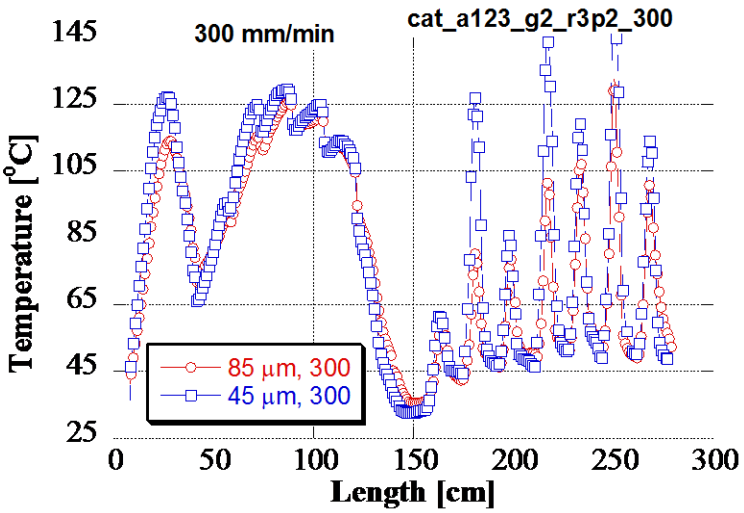

Figure 13. Temperature evolution for coated cathode (final coating thickness was not measured) at 800 mm/min coating speed. The two runs without NCS coating were shown together with the coating run.

Heat flux measurements

Before entering the convection oven, the electrode foil is heated by IR lamps (Figure 14). The heat flux distribution on the electrode foil must be obtained in order to understand the temperature evolution during IR exposure. The electrode foil was inclined with respect to the IR bank (Figure 14). The heat flux sensor was held in a fixture and was positioned at various locations below the IR bank. At each location, the sensor was positioned at the same heights and tilted at the same angle as the electrode foil. The (x, y) positions, at which the heat flux was measured, are shown in Figure 15, where the hashed area indicates the area below the IR lamps. The locations are specified with respect to a system of coordinates whose origin is on the front side of the lamp bank, as the electrode foil is viewed from the slot-die coater: y=-5 indicates the right side of the lamp bank, y=5 indicates the left side of the lamp bank, x=0 indicates the front side of the lamp bank, x=5 indicates the back side of the lamp bank. The data can be grouped in two data sets, one containing those points close to the centerline of the electrode foil, i.e., y=[0:1.25], and the second one containing those points close to the edge of the electrode foil, i.e., y=[3:25:5]. Disregarding the variation in the transversal direction (y), the heat flux for the centerline and edge data sets are shown in Figure 16. The data shows that the peak in the heat flux was recorded at locations towards the center of the IR bank, i.e., x=2 to 3 in, even though the electrode foil is closer to the lamps due to its vertical inclination. The center to edge variation was approximately within 12%. The variation of the heat flux with the power level of the IR system is shown in Figure 17.

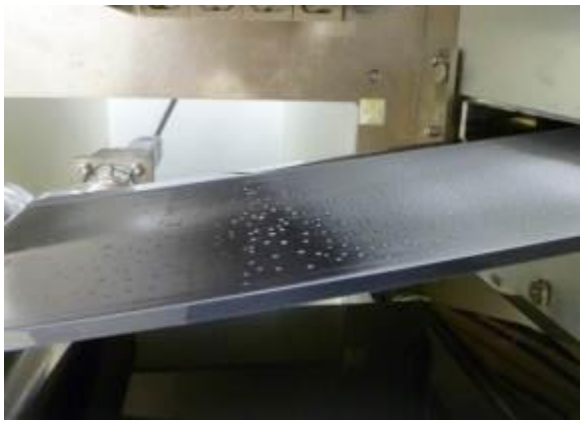

Figure 14. IR lamp bank and electrode foil.

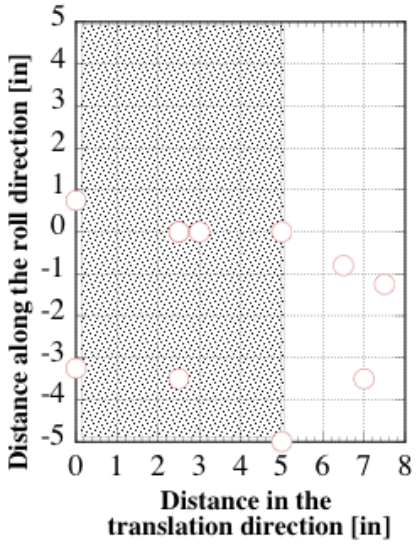

Figure 15. Locations (x,y) at which the heat flux was measured.

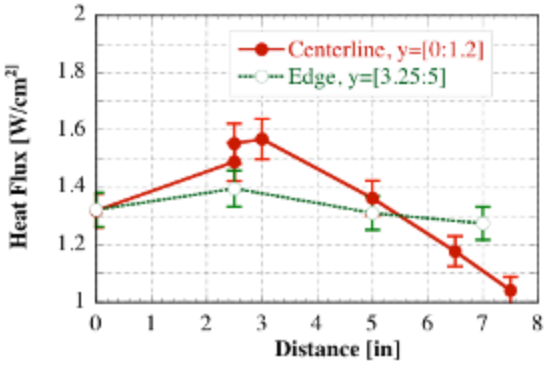

Figure 16. Variation of the heat flux along the electrode foil, i.e., x axis.

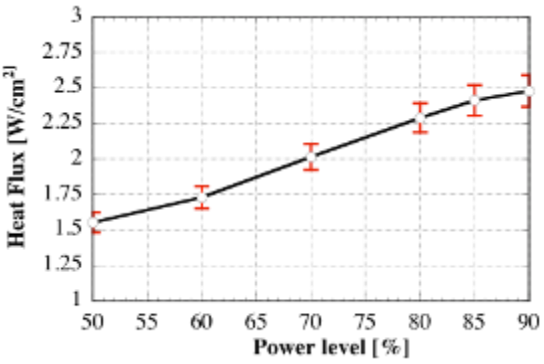

Figure 17. Variation of the heat flux with the power level of the IR system (right below the centerline of the front face of the IR fixture).

Comments and Discussions

The most intriguing feature of the temperature profile is the "V"-like evolution, which occurred as the foil enters the oven. By considering only this temperature drop effect on the drying, without considering any other effects and/or the properties of the multilayered electrode, one may state that this temperature drop may not be desirable. We have to mention that most studies on drying are concerned with isothermal systems, rather than systems in which the temperature varies. However, we would like to mention that it is too early to speculate whether or not this feature would be beneficial or harmful to the NCS coating. Future work will hopefully shed light on the effect of this temperature evolution on the drying of the NCS coating.

4.2 PROCESS MODELING AND SIMULATION

New modules were developed specifically to deal with the drying phenomena of porous media. An existent 3D model for heat transfer and phase changes that was available at ORNL was used as the implementation platform for these new modules. A mass transfer module was developed to account for the evolution of liquid and gaseous phases. The mass transfer module provided data on the temperature within the film. The temperature data was needed to evaluate the extent of drying, i.e., solvent content distribution within the film. The shrinkage and porosity variation had been obtained as the solvent is evaporated and porosity changes. A criterion for cracking had been formulated based on the evolution of shrinkage and temperature gradients.

4.2.1 Radiative Transport Model for Drying Using Infrared Heating

The energy distribution within slurry coatings and substrates that are exposed to radiant energy during drying is important to the dryer operation and control of the surface temperature. A complete set of optical properties for the slurry materials was obtained and then used to evaluate the optical properties of the slurry. A radiative transport model based on spectral two-flux radiation transport equations has been used to simulate the energy transport within semitransparent slurries and coatings. The model can account for the variation of optical properties due to increased particle packing during drying.

Background

Semi-transparent coatings affect the energy balance in web coatings. For example, more reflective coatings would require more energy input to attain the same processing temperatures as those less reflective. It is very important to estimate the reflectivity of the coating system as it undergoes drying by taking into account the optical properties of its different constituents, which include the solvent, particulate matter, and binder. This radiant module will aid to investigate the energy distribution and ensuing temperature evolution during infrared drying. Especially of interest is the ability to control the top surface temperature, as it is in fact the temperature at which solvent evaporates from the coating.

Simple models for radiation transport in translucent materials, such as diffusion approximation models, have been shown to yield unacceptable large discrepancies at the top sample surface, as compared with more rigorous solutions for radiation transport equations (RTE) (Siegal and Howell, 2001). The optical properties can be inferred from the total reflectance and transmittance measurements using two- or four-flux Kubelka–Munk approximations (Levinson et al. 2005). Reviewing the optical properties of particulate systems, several studies that report the optical properties of multilayered paints. Levinson et al. provided data on Kubelka–Munk backscattering and absorption coefficients S and K, and non-spectral forward scattering ratios for 87 pigments over substrates specific to roof paints for wavelengths of 0.3 to 2.5 μm.

4.2.1.2. Coating Constituents and Incident Infrared Spectrum

During drying of a slurry, the amounts of constituents in the coating vary as the solvent evaporates. As an example, Table 2 shows the variation of the volumetric fraction of constituents as the NCS thickness coating decreases from an initial value of 75 μm to its final value of 11 μm. At the end of drying, the coating would have a porosity of 53% and would consist of approximately 21% binder and 26 % solid particles.

Table 2. The evolution of volumetric fraction of the solvent, g_{sol}, binder, g_{bin}, and solid particles, g_p, during drying of an initial slurry thickness of 75 μm and final coating thickness of 11 μm

Coating thickness [μm]	g_{sol}	g_{bin}	g_p
75	93.4	3	3.6
45	88.5	5.2	6.3
17	70.7	13.2	16.1
11	53.0	21.1	25.9

The IR bulbs that were used in the drying experiment were of a "medium-wave" type, with a rated filament temperature of 900 ^{o}C. Thus, the emitted spectrum of the incident radiation is that shown in Figure 18. The data shows that for practical purposes, all of the incident radiation occurs at wavelengths larger than 0.8 μm.

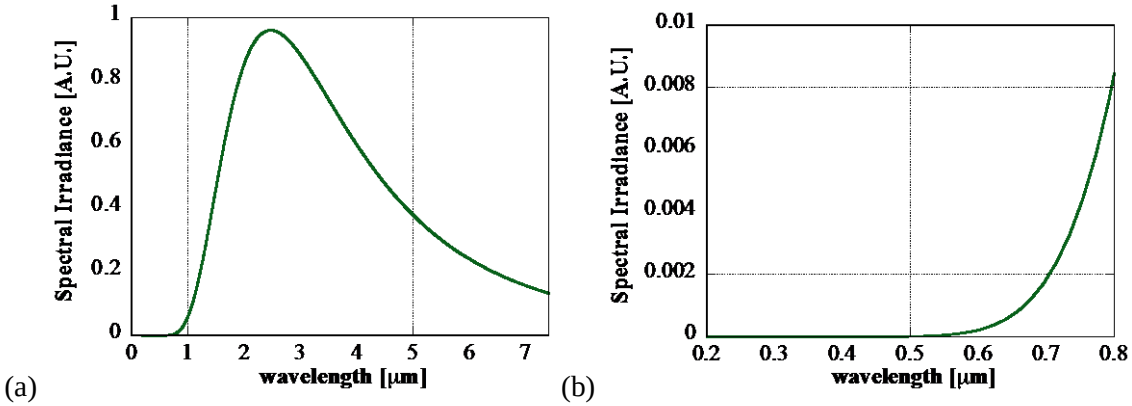

(a) (b)

Figure 18. Spectrum of the incident radiation from the IR lamps: (a) wavelength [0:8] μm, and (b) zoom in on a wavelength domain [0.2:0.8] μm.

Energy Transport Model

In this section, the constitutive equations for the energy transport are presented. The coupling between the radiation transport equations (RTE) and conduction heat transfer is accomplished through the radiative heat flux. The energy equation, which describes the heat transfer, appears as:

$$\rho C_p \frac{\partial T}{\partial t} = \nabla \cdot (k \nabla T) - \nabla \cdot q_r \qquad (1)$$

where ρ, t, k, and T are the density, time, thermal conductivity, and temperature, respectively. The total radiative flux, q_r, is obtained from the radiative transport equations. The boundary conditions include heat transfer losses due to natural convection and radiation at the sample surface. At the outer boundaries of the sample, thermal boundary conditions are imposed such that the heat flux loss is given as:

$$-k \vec{n} \bullet \nabla T = (h_R + h_C)(T_S - T_A) \qquad (2)$$

where $\vec{n}$ is the unit normal in the outward direction from the surface, h_R, and h_C are the heat transfer coefficients due to radiation and convection with the ambient, respectively. T_S and T_A are the

temperature of the sample surface and that of the ambient, respectively, and h_R is given as:

$$h_R\left(T_S - T_A\right) = \sigma\varepsilon\left[T_S^4\left(1 - F_{0\to\lambda cT_S}\right) - T_A^4\left(1 - F_{0\to\lambda cT_A}\right)\right] \quad (3)$$

where σ is the Stefan-Boltzmann constant, λ_C is the cut-off wavelength (i.e., the surface is opaque for $\lambda > \lambda_C$), ϵ is the emissivity of the surface for $\lambda > \lambda_C$. $F_{0\to\lambda T}$ represents fractional blackbody emissive power in the range of 0 to λT [3]. The physical configuration of the layered material consists of air above the sample, then the clear coat, color coat, primer, and electrocoat, respectively.

Two-flux radiation transport equation

Following the Schuster-Schwarzchild approximation, a two-flux radiation model can be obtained for the spectral intensity of the radiation in the forward and backward hemisphere, i_λ^+ and i_λ^-, respectively (Siegal and Howell, Fedorov and Viskanta). For each waveband $\left[\lambda_m : \lambda_{m+1}\right]$, or, $\Delta\lambda_m = \lambda_{m+1} - \lambda_m$, the two-flux approximation for the radiative transport equations (RTE) is given as:

$$\frac{di_\lambda^+}{dx} = -\left(2a_\lambda + \sigma_\lambda\right) i_\lambda^+ + \sigma_\lambda\, i_\lambda^- + 2a_\lambda I_{b\lambda}$$
$$-\frac{di_\lambda^-}{dx} = \sigma_\lambda\, i_\lambda^+ - \left(2a_\lambda + \sigma_\lambda\right) i_\lambda^- + 2a_\lambda I_{b\lambda} \quad (4)$$

where the extinction coefficient is given as a function of the absorption coefficient, a_λ, and the scattering coefficient, σ_λ, by $k_\lambda = a_\lambda + \sigma_\lambda$. $I_{b,\lambda}$ is the intensity of the Plank's black body emission function and, for the medium with index of refraction n and for the waveband $\left[\lambda_m : \lambda_{m+1}\right]$, is computed as: $I_{b,\lambda} = \sigma n^2 T^4\left(F_{0\to\lambda_{m+1}T} - F_{0\to\lambda_m T}\right)$.

Optical Properties

The optical properties were obtained for the materials considered, as follows:

- NMP – considered to be constant at the wavelengths of interest, its value is based on data measured at ORNL at wavelengths [0.2:0.8] μm. The extinction coefficient was obtained from the Fourier transform infrared spectroscopy (FTIR) data obtained from Shui et al. 2006.
- Polyvinylidene fluoride (PVDF, binder) – the index of refraction is considered to be constant at the wavelengths of interest, its value is based on data reported for the PVDF Solef^R at wavelength 0.589μm (Solvey Specialty Polymers). The extinction coefficient was obtained from the data distributed by Atofina for Kynar^R PVDF binders.
- SiO_2 – data available in the Palik database for fused silica.

The index of refraction is shown in Figure 19 while the extinction coefficient is shown in Figures 24a and 24b. The extinction coefficient for quartz is not reported in the Palik database as it is highly transparent at wavelengths [0.16:7.69] μm.

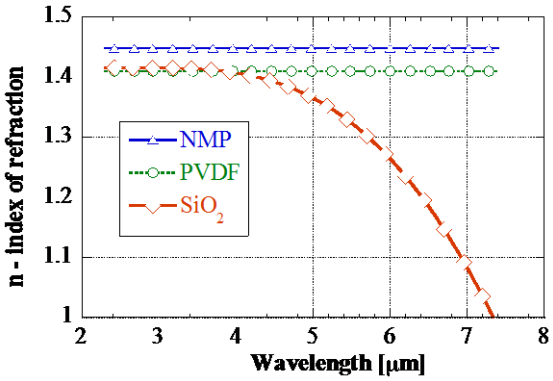

Figure 19. Index of refraction for the materials used in the NCS coating.

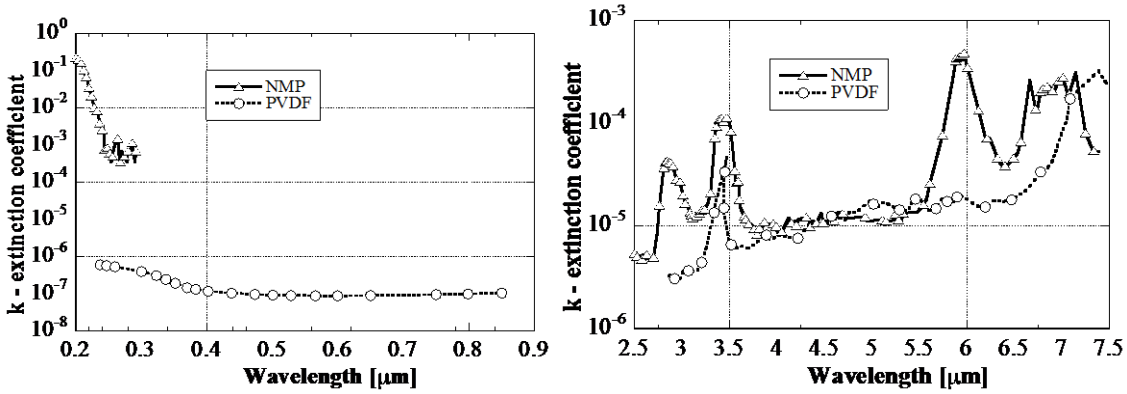

Figure 20. Extinction coefficient for NMP and PVDF (a) NMP- measured at ORNL, PVDF – materials data from Solef[R] brand, (b) NMP – FTIR data obtained from Shui et al. 2006, PVDF materials data from Kynar[R] brand.

Results and Discussion

In this section, the optical properties of the slurry coating were determined based on average models for inhomogeneous media. Initially, the binder is dissolved in the solvent. As drying proceeds, the solvent evaporates and the binder precipitates. At the end of drying, the binder is spread over the surface of the particles and at contact areas between particles. Aside for more complex formulations, it is worth mentioning the use of simple volumetric average for the dielectric constant for coated particles (Alejandro-Arellano et al. 2000) and three-component mixture (Gazdaru and Iorga, 2002). This binder distribution, either coating particles or precipitating as individual particles, makes the evaluation of the optical properties not trivial. However, due to the fact that both the solvent and the binder are highly transparent, as a first approximation, a simple volumetric average formulation was used:

$$\varepsilon^{eff} = \sum_{i=1}^{N} g_i \varepsilon_i \qquad (5)$$

After ϵ^{eff} were calculated using formula 5, the index of refraction and extinction coefficient for the effective medium was calculated from the relationship $n + ik = \sqrt{\epsilon}$. The computed index of refraction for the coating is shown in Fig. 25(a). From the extinction coefficient, the penetration depth can be obtained as wavelength/(4*pi*k). The penetration depth, which is defined as the depth at which the incident irradiation would be decreased by a factor of 1/e, is shown in Figure 21c.

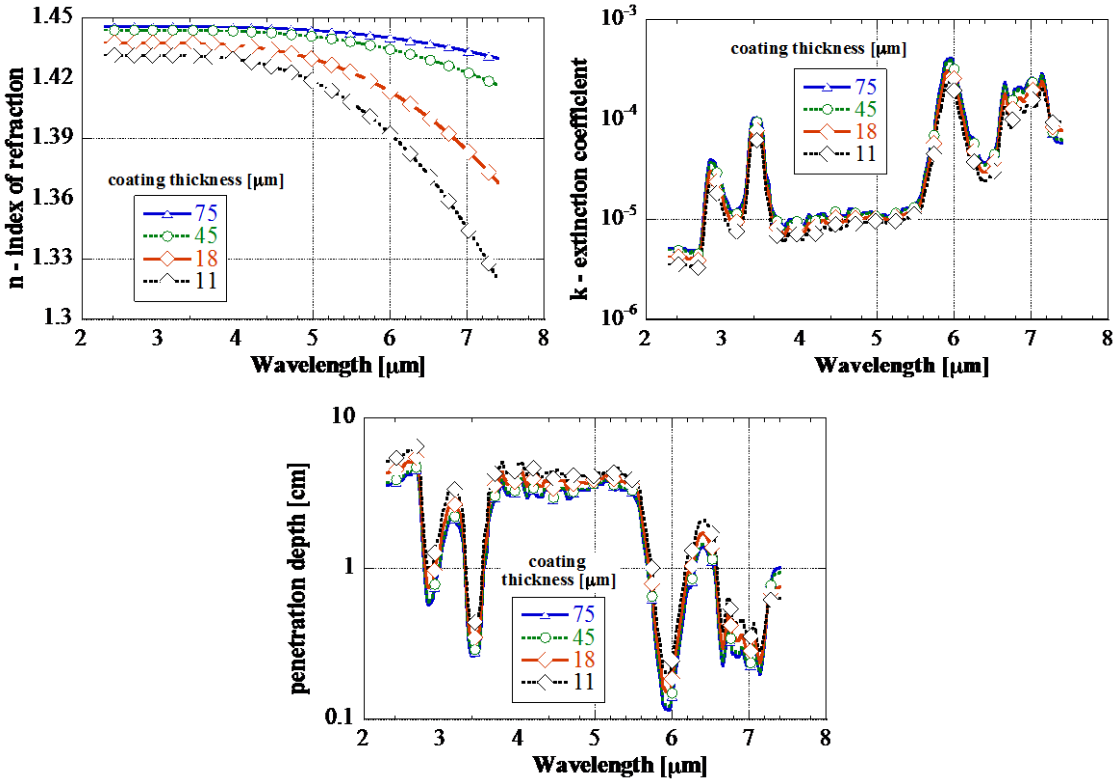

Figure 21. Estimated optical properties for the NCS coating at different coating thicknesses during drying (initial coating thickness was 75 μm): (a) index of refraction, (b), extinction coefficient, and (d) penetration depth (thickness at which radiation intensity would be decreased by 1/e or 36.7%).

The RTE model was run for four cases, at coating thickness of 75, 45, 18 and 11 μm as indicated in Table 2. The index of refraction and extinction coefficient, which are shown in Figure 21 a and b, were used as input in the RTE model. On the backside of the coating sample, i.e., at the interface between the coating and electrode, the emissivity of the uncoated electrode surface was used, rather than the reflectivity given by the optical properties. For uncoated anode, the emissivity was estimated to be approximately 0.85. The results for spectrally averaged absorptivity and reflectivity of the coating and electrode material system considered are shown in Table 3. The results show that the effect of the coating was to increase the effective emissivity from 85% (uncoated anode material) to approximately 81%.

The results also show that little IR energy would be absorbed in the coating (less than 2%). It would be desired to assess what would be the error in predicting the surface temperature using a simple surface absorption of the energy in the coating versus a more detailed model for the energy transport that include the RTE and heat conduction through the coating and other material systems.

Table 3. Total reflectivity, R, absorptivity in the coating, A[%]

Coating thickness [μm]	R [%]	Effective emissivity	A [%]
75	19.04	80.96	1.84
45	19.22	80.78	0.17
17	18.72	81.28	0.28
11	18.58	81.42	0.14

4.2.2 Mass transfer module for drying

A mass transfer module for simulating the drying was developed and its computer implementation complete. In order to handle the variation of coating thickness during drying within the existent 3D software at ORNL, the energy equation is solved over a fixed thickness domain and a coordinate transformation was employed.

The decrease in the amount of liquid phase and the increase in the amount of solid phase within the coating film were considered during drying. Since during drying the solvent evaporates and the coating thickness decreases by almost an order of magnitude to a value that is close to that of the other layers in the electrode, the actual coating thickness has to be taken into account when the temperature is solved for. The coating is assumed to shrink uni-directionally during drying, i.e., in the direction normal to the electrode surface. Since the foil thickness is very small, the heat transfer only through the foil and coating thickness was considered. The foil translation was handled by considering that the top surface of the coating and the bottom surface of the foil are exposed to time dependent conditions that include convection temperatures, radiation temperatures, and convection heat transfer coefficients. Thus, the heat transfer exchange between the foil and rolls was not explicitly considered. Instead, the heat transfer coefficient due to convection was altered to account of this additional cooling due to roll contact.

In summary, the drying module has the following capabilities:

- the shrinkage of the coating is calculated,
- variation of fraction of solids (silica + PVDF) in the coating during drying is considered. As the solvent (NMP) evaporates, the amount of solid fraction increases.
- variation of properties (specific heat, thermal conductivity, density) with the amount of solids in the coating is considered.
- evaporation of NMP is considered based on a simple Hertz-Knudsen equation.

Properties of materials involved (NMP, PVDF, silica) were obtained from open literature. The evaporation of solvent in a mixture of gases atmosphere is still a very active of research and constitutive equations are still under development.

Drying conditions

The coating deposited on the foil is dried using a combination of IR heaters and an oven (Figure 22). A heated pad is placed on the bottom of the oven to provide the radiant heat in the oven. The temperature of the heated pad is denoted as T_{RB} to indicate that the pad would exchange heat by radiation with the foil and other oven components. The air in the oven has a different temperature, Tc, than that of the oven walls. The temperature of the top oven wall is denoted by T_{RB}. Aside from

the ambient temperature, T_{amb}, only T_{RB} was known. Within the entrance and exit transition regions, the variation in heating conditions is not trivial. For example, Tc is not constant but it is dependent on the amount of air at T_{amb} that enters the oven. Also, the thermal radiation conditions are different than those inside the oven, according to the theory of the view factors that may be used to obtain the fractional heat flux exchanged by thermal radiation at each location. In the current model, in order to handle the entrance and exit transition regions, Tc, T_{RB}, and T_{RT} would be varied. The heat transfer exchange between the foil to the rolls was not considered.

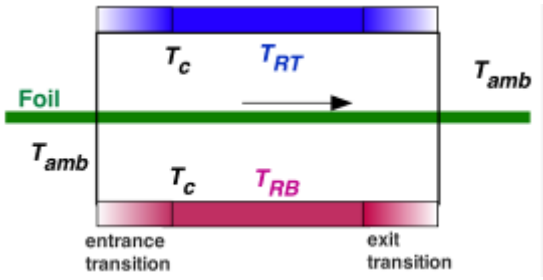

Figure 22. Schematic showing the foil transition regions at the entrance to the oven and exit from the oven. Different temperatures of the oven walls are also shown.

The solid phase is considered to include the binder in addition to the solid particles, while the liquid phase is made of solvent (Figure 23). The following relationships are used to relate the mass fractions, *f*, and volumetric fractions, *g*, of the constituents in the coating through the phase densities and average density, $\bar{\rho}$.

$$\bar{\rho} = g_s\rho_s + g_L\rho_L + g_a\rho_a, \frac{1}{\bar{\rho}} = \frac{f_s}{\rho_s} + \frac{f_L}{\rho_L} + \frac{f_a}{\rho_a}, \quad (1)$$

$$f_i = g_i \frac{\rho_i}{\bar{\rho}}, \quad (2)$$

where *i*=*s*, *L*, and *a* are used as subscripts for the solid, liquid, and air phases, respectively. The air is considered to penetrate into the coating only after the coherency – actual contact between particles, as sketched in the third picture shown in Figure 23. The coherency point has significant implications. For example, the mass flux of solvent is calculated differently before and after coherency. It is considered that before coherency point, the evaporation occurs over the entire surface area of the coating (Figure 23, first and second picture). After the coherency point is reached, the evaporation is considered to occur only through the open area, i.e. that is not obstructed by the solid particles (Figure 23, third picture). Also after the coherency point, the capillary pressure due to the interparticle menisci, would play an important role in the evaporation.

Since the mass of solids is constant, at any given instant, the coating height can be related to the initial height through the volumetric fraction of solids, as:

$$H(t) = H(0)\frac{g_s(0)}{g_s(t)}.$$

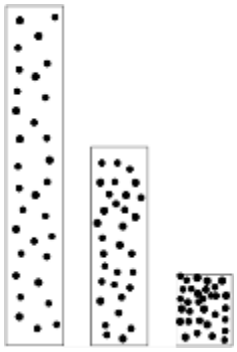

Figure 23. Schematic of solid phase packing as the coating thickness decreases due to solvent evaporation. The third picture represents the coherency point, where the particles touch each other and the coating would be able to support some stress.

The following data was used at the input (Table 4). It was assumed that initially, the coating had 10% solids and that its thickness was 0.2mm. It was also considered the final volumetric fraction of the solids, in pct, was 80%. This high packing fraction can be obtained as the solid phases consist of irregular shaped particles and not of simple spherical particles of uniform size for which the maximum packing fraction is 67%.

Table 4. Data on the initial and final conditions of the coating

Initial coating thickness [mm]	**Final coating thickness [mm]**	**Initial mass fraction of solids**	**Initial volumetric fraction of solids**	**Final volumetric fractions of solids**
$H(0)$	$H(t_f)$	$f_s(0)$	$g_s(0)$	$g_s(t_f)$
0.2	0.0121	0.1	0.0485	0.8

Energy transport model

The energy equation, which describes the heat conduction phenomena for a fixed computational domain, appears as:

$$\bar{r}\bar{C}_p \frac{\P T}{\P t} = \frac{\P}{\P x}\left(k \frac{\P T}{\P x}\right) + \frac{\P}{\P y}\left(k \frac{\P T}{\P y}\right) + \frac{\P}{\P z}\left(k \frac{\P T}{\P z}\right) \quad (3)$$

where ρ, t, and T are the density, time, and temperature, respectively. The overbar indicates average quantities. In order to solve the energy equation on a fixed computational domain, without explicitly tracking the displacement of the mesh vertices within the coating, a coordinate transformation was imposed in the direction that is normal to the electrode surface, say z - direction. The coordinate transformation is:

$$Z = z_0 + (z - z_0)\frac{H_0}{H(t)} \quad (4)$$

where z_0 is the coordinate at which the coating starts, H_0 is a reference thickness, H(t) is the thickness of the coating at the current time, t. This coordinate change is applied only to the coating domain. In

this way, the computational domain is always constant, i.e., from Z=0 on the back side of electrode, to Z=z_0 on the back side of the coating in contact with the electrode, to Z= z_0+H_0 on the top surface of the coating. Employing the coordinate transformation, the energy equation (1) is changed only in the coating domain, as:

$$\bar{r}\bar{C}_p\left[\frac{\partial T}{\partial t} - \frac{\partial T}{\partial Z}\frac{Z - z_0}{H}\frac{dH}{dt}\right] = \frac{\partial}{\partial x}\left(k\frac{\partial T}{\partial x}\right) + \frac{\partial}{\partial y}\left(k\frac{\partial T}{\partial y}\right) + \frac{1}{H^2}\frac{\partial}{\partial Z}\left(k\frac{\partial T}{\partial Z}\right) \quad (5)$$

The right hand side of this equation is to that of the anisotropic heat transfer equation with a thermal conductivity in the Z direction different than that in the x and y directions. Since the coordinate transformation is applied only to the coating domain, the boundary conditions between the coating domain and the electrode layer adjacent to it must be reformulated. The boundary conditions include heat transfer losses due to natural convection and radiation at the foil surface. The boundary conditions are imposed such that the heat flux loss is:

$$q'' = h_R\left(T - T_R\right) + h_c\left(T - T_C\right) \quad (6)$$

where h_R is the heat transfer coefficient due to a radiation temperature of T_R, h_C is the heat transfer coefficient due to a gas convection at a temperature of T_C. T is the temperature of the sample surface. In this work, h_C was varied in each regions and:

$$h_R = se\left(T^2 + T_R^2\right)\left(T + T_R\right) \quad (7)$$

where s is the Stefan-Boltzmann constant and e is the emissivity of the sample surface. The data on thermophysical material properties is shown at the end of this section.

Empirical Models for the Evaporation Rates

The amount of solvent evaporation can be evaluated using Langmuir-like equations. The Langmuir equations relate the outgassing rate and the vapor pressure of a homogenous monomolecular weight material in high vacuum (Heslin, 1977). The net evaporated mass flow rate, $\dot{m}$, is the difference between the evaporated and condensed mass flow rate. Neglecting the partial pressure of the evaporated gas phase of the solvent at larger distances from the surface, the evaporated $\dot{m}$ is given based on Hertz-Knudsen equation as a function of the surface temperature, Ts, saturated vapor pressure, Ps (corresponding to Ts), and universal gas constant, R, as:

$$\dot{m}_e = bP_s\sqrt{\frac{M}{2pRT_s}}, \quad \textbf{(8)}$$

where β is an empirical evaporation coefficient that needs to be determined experimentally or through molecular dynamics simulations and the saturated vapor pressure is given by the Clausius-Clapeyron equation, as:

$$P_s(T) = P_o\exp\left[-\left(1/T - 1/T_o\right)H_v/R\right] \quad (9)$$

The contribution of air molecules to the general kinetic theory for evaporation within the Knudsen layer has yet to be considered.

During a time step, Δt, the solvent fraction, g_L, would decrease based on the evaporated mass flux of solvent, ΔQ_L, as:

$$g_L(t+\Delta t) = g_L(t) - \Delta Q_L \frac{1}{H(t)\varrho_L}, \quad (10)$$

The mass flux of solvent is calculated differently before and after coherency. It is considered that before coherency point, the evaporation occurs over the entire surface area of the coating (Figure 22, first/second picture). After the coherency point is reached, the evaporation is considered to occur only through the open area, i.e. that is not obstructed by the solid particles (Figure 22, third picture). Thus, before the coherency point, the mass flux of solvent is given by the solvent mass evaporation rate, as:

$$\Delta Q_L = \Delta t \, \dot{m}_L \quad (11)$$

After the coherency point, the mass flux of solvent is related to the solvent mass evaporation rate though the following relationship:

$$\Delta Q_L = 0.3 \, (1 - g_s) \Delta t \, \dot{m}_L, \quad (12)$$

where the $1 - g_s$ factor is used to account for the open area for evaporation and 0.3 is an empirical factor used to account for the capillary pressure effects, as they are not considered in this current model implementation.

Models for Evaporation Rates based on Correlations for Mass Transport Coefficients

Efforts were made to enhance the evaporation model in order to predict the evaporation rates under both lab and actual plant conditions. The empirical model for the evaporation rates does not account for differences between the forced convection and natural convection (Table 5).

Table 5. Mass transport coefficients

Evaporation rate	***Model/Data***	***Reference***	***Comments***
Hertz-Knudsen	evaporation coefficient not provided	Heslin (1977)	Forced convection not handled
Mass transfer coefficient for natural convection	Correlation for natural convection; diffusion coefficient of NMP in air	Bouyer et al. (2010)	Representative for IR heating region and first furnace
Mass transfer coefficient forced convection	Correlation for evaporation rate under forced convection	Atakan and Can (1999), Yip, A.J. McHugh (2006)	Representative for second furnace

Employing the same coordinate transformation as for the energy equation, the diffusion equation within the coating domain becomes, as:

$$\frac{\partial c_1}{\partial t} = \frac{Z - z_o}{H}\frac{dH}{dt}\frac{\partial c_1}{\partial Z} + \frac{\partial}{\partial x}\left(D_1 \frac{\partial c_1}{\partial x}\right) + \frac{\partial}{\partial y}\left(D_1 \frac{\partial c_1}{\partial y}\right) + \frac{1}{H^2}\frac{\partial}{\partial Z}\left(D_1 \frac{\partial c_1}{\partial Z}\right) \quad (1)$$

The boundary conditions at the coating surface are expressed in terms of mass fluxes [Kg/m^2 s] in the gas phase, as:

$$J_{1,g} = -\frac{D_1}{H}\frac{\partial c_1}{\partial Z} = k_1\left[c_{1,g}(T) - c_{1,g\infty}(T_g)\right], \quad (2)$$

where $c_{1,g}$ is the concentration of component 1 at the tape surface (i.e., air-coating interface) at the

coating temperature T. $c_{1,g\infty}$ is the concentration of component 1 in the gas phase at the gas temperature, T_g. In this study, $c_{1,g\infty}$=0 for well ventilated enclosures. D_1 is the diffusion coefficient in the NMP-PDVF based coating which is in the liquid state. k_1 is the mass transport coefficient [m/s].

Correlations for the mass transfer coefficient under *natural* convection regimes, are given as (Bejan, 2004; Tsay and McHugh, 1991) by substituting in heat transfer correlations Nusselt numbers with Sherwood numbers (Nu->Sh) and Pr with Sc (Pr->Sc). A similar procedure can also be used for the forced convection regime. The mass transfer coefficient correlations can be given, as:

$k_1 \frac{L_c}{D_{1,g}} y_{1,g}^{log,m} = 0.27(Gr\ Sc)^{0.25}$, for natural convection (7)

$k_1 \frac{L_c}{D_{1,g}} y_{1,g}^{log,m} = 0.27 Re^{0.5} Sc^{0.5}$, for forced convection (8)

where L_c is a reference length, given in this case by the tape width and $D_{1,g}$ is the diffusion coefficient of NMP in air. By definition, the Schmidt number, Sc, and Reynolds number, Re, are:

$$Sc = \frac{\mu_g}{\rho_g D_{1,g}} \text{ and } Re = \frac{\rho_g U L_c}{\mu_g} \quad (9)$$

The Grashof number, Gr, depends on the density gradients of the gas phase between the gas away from the air-coating interface and at the air-coating interface. Both the temperature and the concentration of the gas phase are considered to estimate Gr number, as:

$Gr = \frac{\rho_g^2 g L_c^3}{\mu_g^2}\left[\beta_T\left(T - T_{g\infty}\right) + \beta_y\left(y_{1,g} - y_{1,g\infty}\right)\right]$, (3)

$\beta_T = -\frac{1}{\rho_g}\left(\frac{\partial \rho_g}{\partial T}\right)_{P,y}, \beta_y = -\frac{1}{\rho_g}\left(\frac{\partial \rho_g}{\partial T}\right)_{P,T}$ (4)

$\frac{Gr}{L_c^3} = \frac{\rho_g^2 g \beta_T}{\mu_g^2}\left(\Delta T + \frac{\beta_y}{\beta_T}|\Delta y|\right)$ (5)

The "0.27" coefficient takes values of 0.54 and 0.14 when 10^5 < Gr Sc < $2x10^7$ and $3x10^7$ < Gr Sc< $3x10^{10}$, respectively. It has to be noted that the diffusion coefficient was evaluated at the average temperature, i.e., $0.5\left(T_g + T_s\right)$. The following relationships are used to relate the mass fractions, *f*, and volumetric fractions, ϕ, of the constituents in the coating through the densities of each species and average density, $\bar{\rho}$.

$\bar{\rho} = \sum_{j=1}^{N} \phi_j \rho_j, \frac{1}{\bar{\rho}} = \sum_{j=1}^{N} \frac{f_j}{\rho_j}$, (3)

$f_j = \phi_j \frac{\rho_j}{\bar{\rho}},\ c_j = \phi_j \rho_j, f_j \bar{M} = y_j M_j, \bar{M} = \sum_{j=1}^{N} y_j M_j$ (4)

where *j*=1, 2, or 3 is used as subscript for the NMP, PVDF, and solid phases, respectively. For the gas phase:

$p_j = y_j p$, and $\bar{\rho} = \frac{p}{RT}\left(\sum_{j=1}^{N} y_j M_j\right)$. (5)

Using the definitions for average density of air-solvent mixture, β_T=1/T and $\beta_y = \frac{|M_1 - M_{air}|}{\bar{M}}$, where $\bar{M}$ is evaluated at the film conditions, i.e., at $y_{1,f} = \left(y_{1,g} + y_{1,g\infty}\right)/2$, as: $\bar{M} = y_{1,f} M_1 + \left(1 - y_{1,f}\right) M_{air}$. For air at temperatures between room temperature to 100 °C, the average Prandtl number is Pr=0.7. Other quantities involved in natural convection correlations are given in Table 6.

Table 6. Properties of dry air for obtaining the temperature variation effects on natural convection (Bejan, 2004)

Temperature [^{o}C]	$\frac{\rho_g^2 g \beta_T}{\mu_g^2}$ [1/(cm^3 K]	β_T [1/K]
0	205	0.00366
10	173	0.00352
20	148	0.00340
30	126	0.00331
60	79	0.00299
100	48	0.00269
200	13	0.00165

The mole fraction at the gas side of the air-coating interface, $y_{1,g}$, is determined based on relationships involving the gas concentration. The log mean mole fraction difference (LMmfD) of air, $y_{air,g}^{log,m}$, which is evaluated for the surface, $1 - y_{1,g}$, and bulk stream conditions, $1 - y_{1,g\infty}$, is given as:

$$y_{air,g}^{log,m} = \frac{(1-y_{1,g})-(1-y_{1,g\infty})}{\ln\left(\frac{1-y_{1,g}}{1-y_{1,g\infty}}\right)} \quad (10)$$

All the properties related to the diffusion phenomena are included at the end of this section.

Results for the evaporation rates of the solvent under infrared heating

In this section, experimental data was presented for the drying of pure NMP solvent in a natural convection regime as during infrared (IR) heating. This data can be used to understand the high drying rates that are exhibited by NMP solvent during IR. This study also provides useful evaporation mass flux data that can be used for the design of IR assisted drying systems. Correlations that were used in the literature for predicting mass transport coefficients and evaporated mass fluxes are presented. This section summarizes the data and findings from our study (Sabau et al., 2012), in which it was found that the calculated evaporated mass fluxes are approximately one order of magnitude less than those measured.

Experimental data was presented for the drying of pure NMP solvent in a natural convection regime as the solvent surface and substrate were heated by infrared lamps (Sabau et al., 2012). Correlations that were used in the literature for predicting mass transport coefficients and evaporated mass fluxes are presented. It was found that the calculated evaporated mass fluxes are approximately one order of magnitude less than those measured. This data can be used to understand the high drying rates that are exhibited by NMP solvent during IR exposure. This study also provides useful evaporation mass flux data that can be used for the design of IR assisted drying systems.

The experimental setup considered allowed only the IR heating of the sample. The drying rate was estimated from the measured weight loss during a drying experiment of pure NMP. The experiments were conducted in still air, thus the only air-flow would be that established by the natural convection due to hot foil. A droplet of 100 μL of pure NMP was dropped on an aluminum foil container, whose

sides were approximately 5 cm and thickness was 20 μm. The pipette mass was calibrated at 91.83 mg of NMP. The aluminum foil was placed on a Mettler Toledo XS603S precision balance. According to the manufacturer, the balance had the following precision specifications: 1 mg readability, 0.9 mg repeatability, and 1.5 s settling time. Several experiments were conducted in order to insure the reproducibility of the data. Typical weight loss curves and temperature variations during drying are shown in Figure 24. The raw signal from the microbalance (Figure 24(a)) was integrated and scaled such that the total evaporated mass was equal to that of the NMP droplet. The evaporated mass as a function of time is given in Figure 24(b). From the data shown in Figure 24, the mass loss rate was estimated to be 1.30767×10^{-3} g/s. For a droplet area of 7.24 cm^2, the evaporated mass flux becomes 1.8062×10^{-4} g/(cm^2 s). Initially, the film thickness was estimated to be 123.3μm.

During the drying experiment, the temperature was measured using a thermocouple that was placed on top of the Al foil, close to the NMP surface. The top surface thermocouple shows an average temperature variation of approximately 83 ^oC (Figure 24(c)). Since from our past experience, IR can overheat directly this top surface thermocouple, an additional experiment was conducted, after the drying study was completed, in which an additional thermocouple was wrapped into one side of the Al foil. The surface thermocouple, which was placed on top of the aluminum foil showed temperatures higher by 6 ^oC than that by the thinner gauge thermocouple embedded into the Al foil.

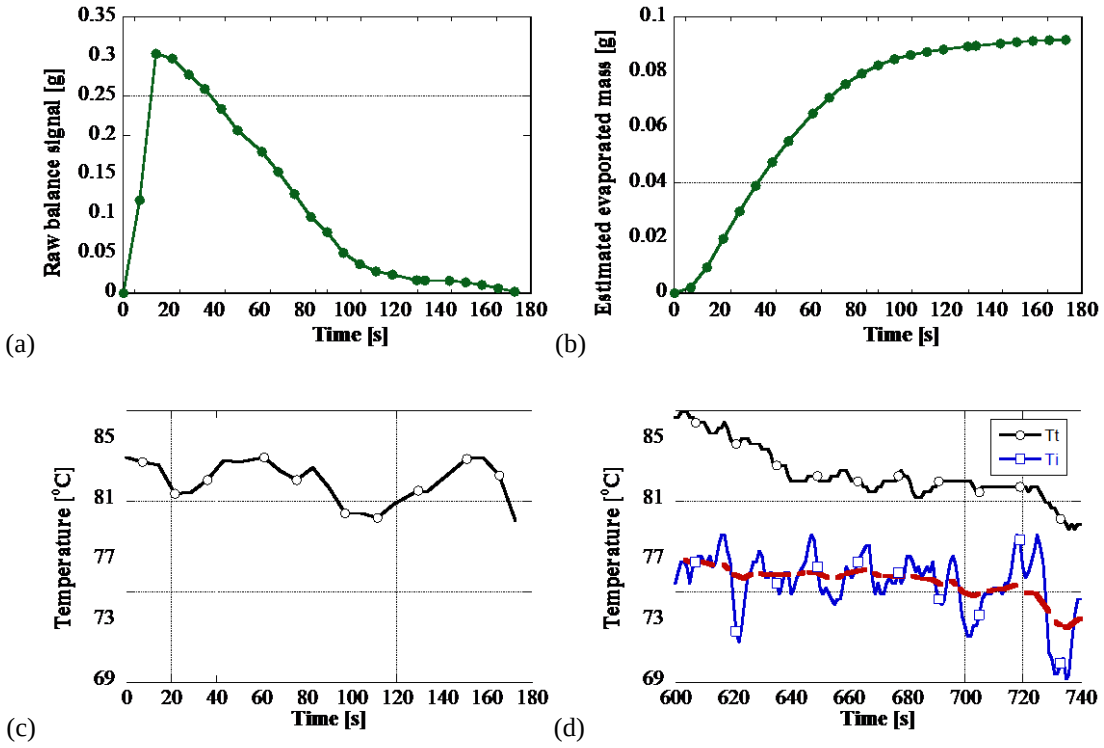

Figure 24. Typical data during drying: (a) raw micro-balance signal [g] and (b) estimated weight loss and (c) temperature variation and (d) temperature variation for both the top thermocouple and another thermocouple wrapped into one side of the Al foil.

In the first case considered, the surface temperature –or the evaporation temperature – was considered to be that of the Al foil, 77 ^oC, i.e., without considering that the IR radiation would increase it. In this respect, the results shown in Table 3, indicate that the natural convection is in the laminar regime and

the computed evaporation mass flux, $\dot{m}_{nc}$=1.471x10^{-5} g/(cm^2 s), is much smaller than the measured value of 1.8062x10^{-4} g/(cm^2 s). This ratio between the measured evaporation mass flux and that given by natural convection correlations is approximately 12.3 and 8.8 when the surface temperatures were considered to be 77 ^{o}C and 83 ^{o}C, respectively. It has to be mentioned that the ratio between the mass fluxes without and with IR, can be estimated based on the correlation for the combined radiation and *forced* convection presented by Jaturonglumlert and Kiatsiriroat (2010) to be approximately 5.

Numerical simulation results for drying

One of the most important factors that describe the evaporation rate in the simplified formulation for the drying rate is the empirical factor, β. This parameter describe the deviation of the evaporation flow rate from that predicted by Hertz-Knudsen equation. Ultimately, this parameter has to be determined from experimental data and other models considered for the evaporation rate.

Since data on convection temperatures, radiation temperatures, and heat transfer coefficient due to convection are not available for the all the regions in the oven, they were varied until a good agreement was obtained between the measured data for the back side temperature and a case in which β=1.0e-5 (Figure 25). The data in Figure 25 shows that the temperature of the top surface of the coating, T_S, is higher than that of the back side foil, T_B; while in the oven, $T_S < T_B$. These two types of differences between T_S and T_B were observed in experimental results. The data was shown as a function of both foil length, as measured from the first roll, and time as this data may be used for other experimental studies of drying or to obtain actual evaporation rates during a static experiment. For β=1.0e-5, the drying was incomplete.

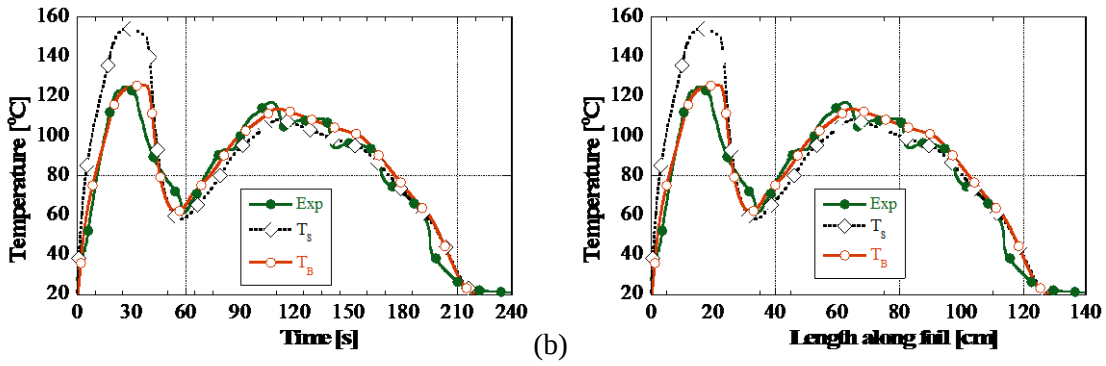

(a) (b)

Figure 25. Experimental and computed temperature results for the drying of a coating on an anode foil at 35 cm/min foil speed (β=1.0e-5).

Then β was increased, as shown in Table 7, in order to attain complete drying. The results for two cases are shown in detail in Figures 30, 31, and 32. The results shown in Figure 26 show that in this case for which for β=5.0e-4 the drying occurs very fast. Since so much solvent is evaporated, the temperatures in the foil drop. The temperatures rise once the heat flux due to the evaporation vanishes after the evaporation is complete. This case may be unrealistic, as the sharp drop in the peak temperatures is not evidenced in the experimental results. In Figure 26b, the results for the fractions of phases (solvent, solids, and air) are shown. The results show the fast drying that occurred as the foil displaced from the 15 cm location to the 18 cm location. At about 18 cm, the second regime of drying, i.e., the drying after the coherency has been reached proceeds. In this regime, the fraction of solids stays constant and the air enters the coating as the solvent evaporates. In Figure 26c, the

evolution of the coating thickness is shown. After the coherency point has reached, the coating does not shrink any more due to evaporation.

In Figure 27, the results are shown for the case in which β=1.5e-4. Again the coherency point and the second drying regime can be identified from the data shown for the fractions of solvent, solids, or air (Figure 27b). The data with respect to the foil length is shown in Figure 27. For the sake of completion, the data shown as a function of time is shown in Figure 28 for the same case.

Table 7. Cases considered for the evaporation coefficient β

β, empirical evaporation coefficient	*Foil length at which drying is complete [cm]*	*Comments*
1.0e-5	-	incomplete drying
1.0e-4	-	incomplete drying
1.0e-3	16	drying complete before oven entrance
5.0e-3	10	drying complete before oven entrance
5.0e-4	20	drying complete before oven entrance
2.0e-4	65	drying complete close to the 3-rd roll in the oven
1.5e-4	86	drying complete close to the 4-th roll in the oven

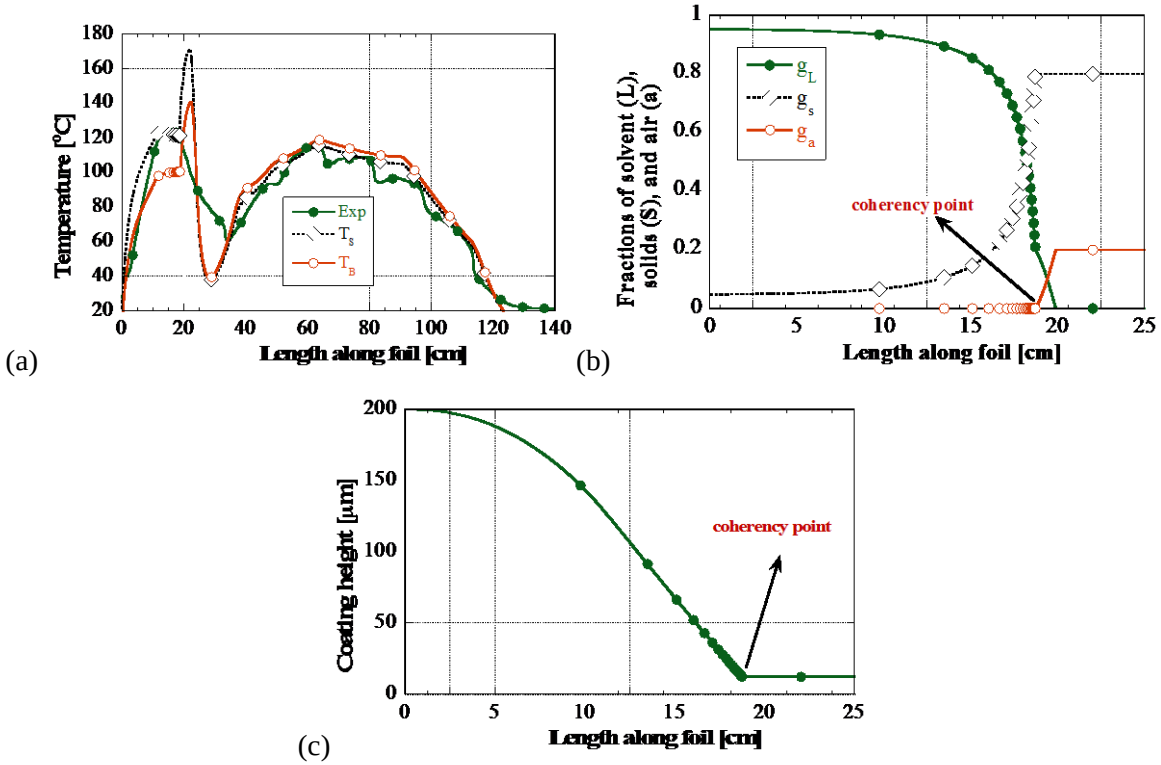

Figure 26. Drying of a coating on an anode foil at 35 cm/min foil speed (β=5.0e-4): (a) experimental and computed temperatures; (b) fractions of solvent (L), solids (S), and air (a); and (c) coating thickness.

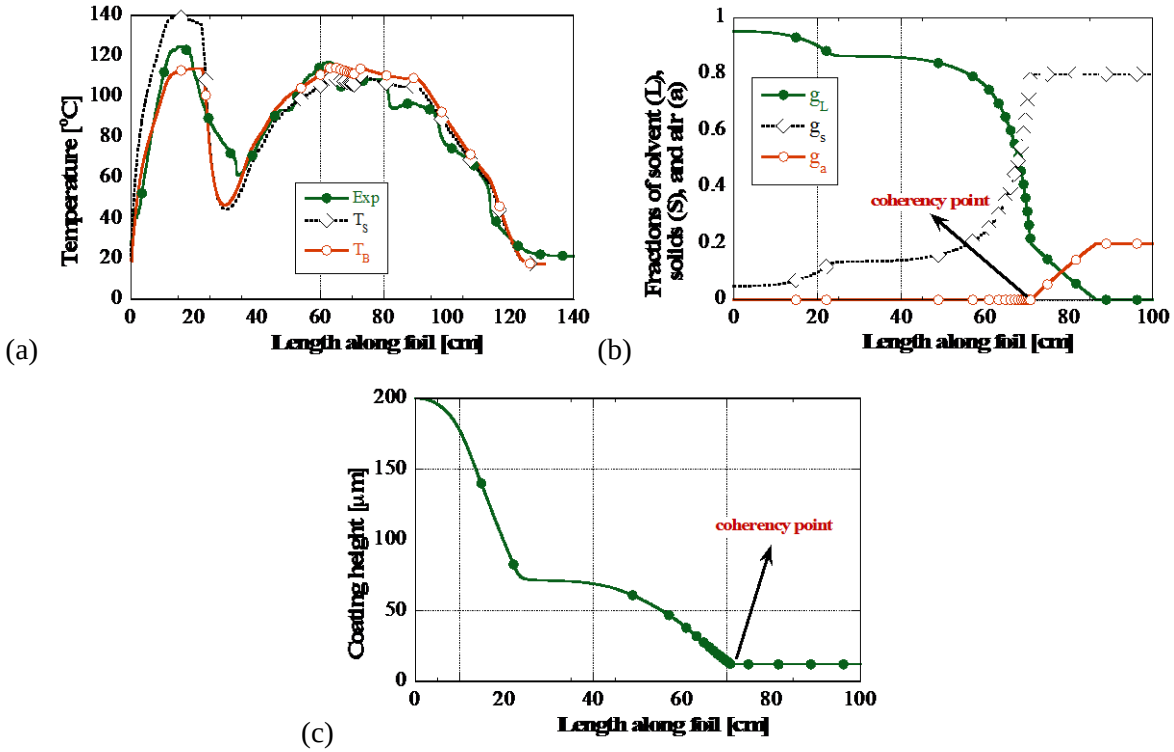

Figure 27. Drying of a coating on an anode foil at 35 cm/min foil speed (β=1.5e-4): (a) experimental and computed temperatures; (b) fractions of solvent (L), solids (S), and air (a); and (c) coating thickness.

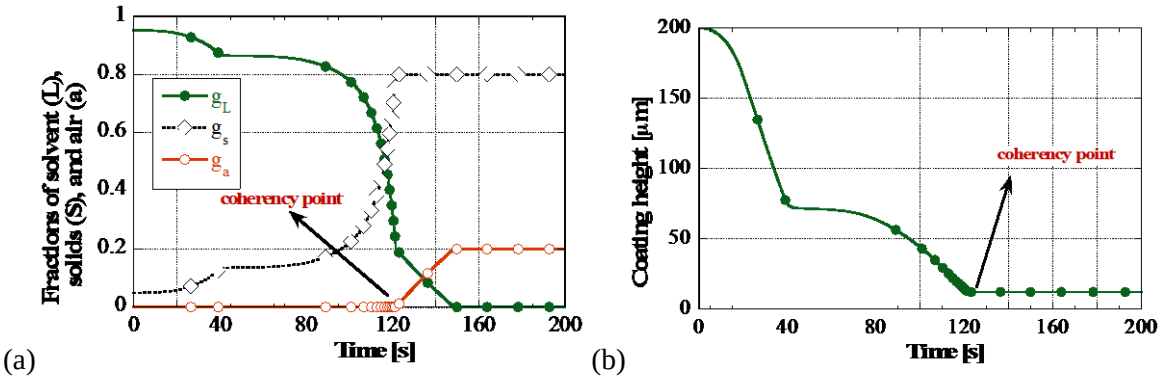

Figure 28. Time dependence results for drying of a coating on an anode foil at 35 cm/min foil speed (β=1.5e-4): (a) computed fractions of solvent (L), solids (S), and air (a); and (b) computed coating thickness.

Results for the mass transport coefficients

Results for the evolution of solvent content – referred to as moisture content in most studies – was obtained in this section based on correlations for the mass transport coefficients for the drying of the NCS coating. Specifically, natural convection correlations were used in this section. We have to mention that Sabau at al. (2012) showed, based on experimental data that was discussed in previous sections, that mass transfer transport coefficient for the natural convection regime when IR heating

was approximately between 9 to 12 times than that evaluated based on natural convection correlations. Thus, in this section, the mass transport coefficient was increased 12 times in the IR heated region than that estimated by the natural convection correlations was considered. Moreover, the mass transport coefficient in the oven had also to be increased by 5 times in order to attain an acceptable drop in the solvent content within the drying oven. This increase is likely due to the difference between the conditions for which the mass transport coefficient were derived and actual conditions in the oven. Understanding how the actual oven conditions, geometry, etc. affect the mass transport correlations, in a similar fashion to the understanding of the differences in the IR heated region, was beyond the scope of this effort.

This drying data was obtained in this section considering that the temperature profile for evaluating the air properties, which are used in the correlations, is that given in Figure 29. Results for the mass transport coefficient for the drying of the NCS coating using natural convection correlation are shown in Figure 30. A very small amount of residual NMP was predicted at the end of the drying oven. This is somehow likely due to the fact that there are small pores in the NCS coating, pores from where the evaporation would be very difficult under the current temperature conditions. Further efforts to understand the mass transport within drying ovens, such as the one at A123, which was used in this study, would be required to establish strong evaporation rate correlations based on the variation within specific sections in the oven of the geometry and temperature.

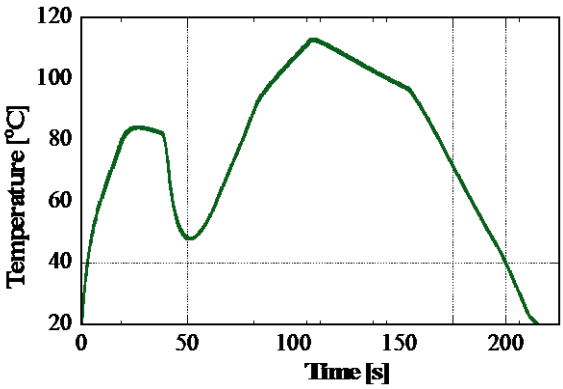

Figure 29. Estimated average air temperature, $0.5(T_g + T_s)$, used to evaluate properties for estimating natural convection effects.

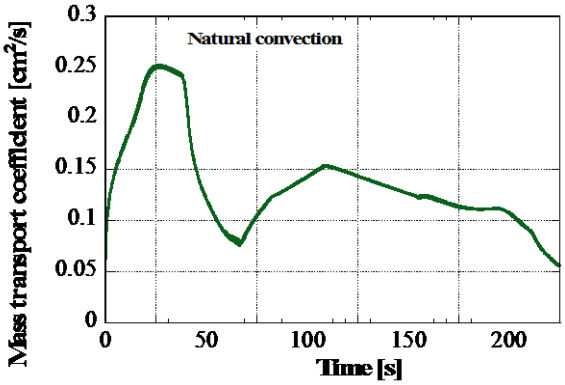

Figure 30. Preliminary results for the mass transport coefficient for drying of the NCS coating using natural convection correlations.

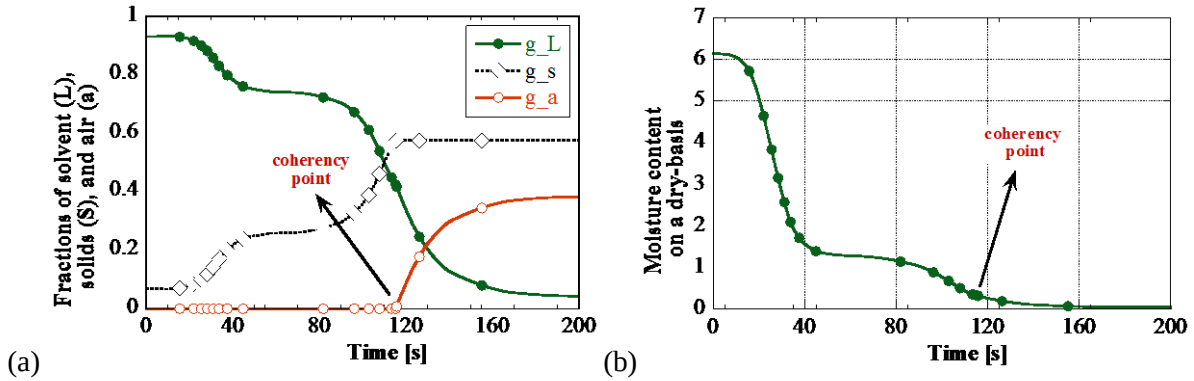

(a) (b)

Figure 31. ***Time dependence*** **results for drying of a coating on an anode foil at 35 cm/min foil speed using evaporation rates based on mass transport coefficients: (a) computed fractions of solvent (L), solids (S), and air (a); and (b) computed coating thickness.**

Thermophysical Materials Properties

Thermophysical properties, such as specific heat, thermal conductivity, density, thermal expansion are required for the mass and heat transport simulations. The electrode properties were those measured by Maleki et al. (1999), if not otherwise specified. DSC measurements showed that PVDF starts melting at about 130 ^{o}C and completed at approximately 173 ^{o}C (dos Santos et al., 2008).

The latent heat of vaporization of NMP is 44.45 kJ/mol at its boiling point of 477 K (Kneisl and Zondlo, 1987). The thermophysical properties of the NMP solvent were those from Grujicic et al. (2003). The molar mass of NMP is 99 g/mol. The partial pressure of NMP is given by the following expressions involving Antoine coefficients (Kneisl and Zondlo, 1987), as:

$$P_s[bar] = exp\left(9.62482 - \frac{3811.448}{T[K]-80.355}\right) \quad (6)$$

Table 8. Thermophysical properties

Material	ρ **[Kg/m^3](density)**	**Cp [J/Kg K] (specific heat)**	**k [W/m K] (thermal conductivity)**	**Reference**
NMP (liquid phase)	1,030	1,680	1.79	Grujicic et al. (2003).
NMP (gas phase)	-	1,260	1.79	Grujicic et al. (2003).
PVDF	1,700 (mean)	1,325 @ 25 C 1,878 @ 117 C	0.21 (mean)	Iguchi et al. (2007); dos Santos et al. (2008)
Fused silica	2.65	703	1.3	

Other properties of dilute solutions of poly(vinylidene fluoride) (PVDF) in N-methylpyrrolidone (NMP) were measured by Ambrosone et al. 1991.

Diffusion-related properties

Diffusion coefficients, densities, and viscosities have been measured for dilute solutions of poly(vinylidene fluoride) in N-methylpyrrolidone. The results have been briefly discussed with the aid of Flory-Huggins and Stokes-Einstein equations (Ambrosone et al. 1991). The diffusion coefficient was measured at 20 ^{o}C for the NMP-PVDF system to be:

$$D_{1,L}[\mathrm{cm}^2/\mathrm{s}]\,10^6 = 0.049 + 12.84 f_2 - 89.7(f_2)^2, \quad (14)$$

where f_2 is the weight fraction of PVDF in the coating.

The temperature dependence of the diffusion coefficient can be given, as:

$$D_{1,L} = D_{1,L}^{o} e^{-E_o/RT} \quad (15)$$

In the air, the diffusion coefficient [cm^2/s] of NMP is given as:

$$D_{1,g}(T) = \frac{1.43\times 10^{-3} T^{1.75}}{P\sqrt{M_{1,g}}\left[76.74^{1/3}+19.7^{1/3}\right]^2} \quad (16)$$

where $M_{1,g} = 2M_1 M_{air}/(M_1+M_{air})$ and P is the gas pressure [bar]. For atmospheric pressure and for NMP, this results in $M_{1,g} = 44.86$ g/mol and:

$$D_{1,g}(T) = 4.42 \times 10^{-6} T^{1.75}\ [\mathrm{cm}^2/\mathrm{s}]. \quad (17)$$

The activity coefficient for NMP in the NMP-PVDF solution is evaluated using the following expression that was derived from the Flory-Huggins theory for the chemical potential of a binary mixture of NMP and PVDF (Ambrosone et al. 1991; Yip and McHugh, 2006), as:

$$a_1 = \phi_1 \exp\left[\phi_2\left(1 - \frac{M_1}{\rho_1}\frac{\rho_2}{M_2} + \chi\phi_2\right)\right] \quad (18)$$

where Flory-Huggins interaction coefficient χ=0.425 (Ambrosone et al. 1991) and molar mass of PVDF was M_2=450,000 g/mol. Since M_2>>M_1, the activation coefficients becomes:

$$a_1 = \phi_1 \exp[\phi_2(1+\chi\phi_2)]. \quad (19)$$

Assuming ideal gas and thermodynamic equilibrium (Yip and McHugh, 2006), the NMP concentration at the gas side of the air-coating interface, $c_{1,g}$, can be given as a function of the solvent activity on the coating side, a_1, as:

$$c_{1,g} = \frac{a_1 P_{sat}}{P}\rho_1 \quad (20)$$

The mole fraction at the gas side of the air-coating interface, is determined using the following set of equations, as:

$$\phi_{1,g} = c_{1,g}/\rho_1;\ \phi_{air,g} = 1 - \phi_{1,g},\ \bar{\rho} = \phi_{1,g}\rho_1 + \phi_{air,g}\rho_{air}(T), \quad (21)$$

$$\bar{M} = \frac{RT}{p}\bar{\rho},\ \text{and}\ y_{1,g} = c_{1,g}\frac{\bar{M}}{M_1}\frac{1}{\bar{\rho}} \quad (22)$$

4.2.3. Stress Model

A comprehensive model for stress analysis during drying of a coating on flexible substrates was developed. The model takes into account the binder role on mechanical properties of the coating and electrodes, especially the different behaviors in tension and compression states. The development of the coupled fluid flow and stress module was complete. The solution algorithm for solving the new stress-strain equations for drying of a coating on flexible, multiple layered substrates was developed. Averaging techniques for the evaluation of Young's modulus, Poisson's ratio, and coefficient of thermal expansion of mixtures were reviewed. The stress-strain model was developed by reviewing experimental data for similar systems as well as recent advances in the poroelasticity theory.

Stress analysis results were presented after coherency point was reached in the coating and after the liquid menisci start to form at the top surface of the coating, when the coating is also subject to the capillary pressure from the top surface. Numerical simulation results were presented for the evaluation of the mechanical properties of the coating, such as Young's modulus. The results show that tensile stresses in the coating are possible. These tensile stresses are likely responsible for the cracking of coatings.

These preliminary simulations were conducted for small values of the Young's modulus. Future cases will aim at using more realistic values for the materials properties, such as Young's modulus, limits for the coherency point, and limits for the menisci formation. Finally, the stress levels and the strain levels will be compared with those for the plastic yield of the coating and failure criteria.

Two concepts were also reviewed in this report that can be used to assess the propensity to cracking of coatings. One property that is relevant to the coating damage is the tensile strength of the solid matrix, which must include the effect of the binder. The data on the temperature dependence of the yield stress of the binder was found. The second cracking criterion is based on linear elastic fracture mechanics.

Nomenclature

g_L - volume fraction of solvent,

$g_a(t,z)$ - volume fraction of air,

W(t) - moisture content on a dry-basis

T – temperature,

t – time,

z- vertical coordinate normal to the coating,

Approach

In order to develop a comprehensive model for dealing with stress evolution during a film drying, the models for following phenomena/properties must be considered:

1. binder effect on elastic properties of the coating
2. elastic properties of non-homogeneous media
3. particle packing and solvent capillary effects
4. stress-strain formulations for coating drying

Binder effect on the elastic properties of the electrode

From a mechanical point of view, the binder provides strength to the solid particles, keeping them in contact when locally they are subjected to tensile stresses. It is thus considered here, that the binder properties would govern the elastic properties of the electrode when in tension while the solid particles and binder would both affect the elastic properties in compression. Thus, the electrode is expected to have different elastic properties in tension and compression. This concept is supported by experimental data presented by Babinec et al. (2007), where data is shown for standard testing of micro-tensile bars and nano-indentation (compressive test) of $LiCoO_2$/PVDF thin films.

There are very few studies on elastic properties of packed bed of particles in which binders are used. In this rare study, Hancock et al. (1993) presented data on Youngs modulus as well as critical stress intensity factor, K_{IC}, for PVP and HPMC binders and glass particles. The tests were conducting using a four-point bending test. The data shows that for the four-point bending testing, in which some parts of the bound powder compact was in tension and parts in compression, varied from approximately 2 to 5 GPa and in some instances from 0.4 to 2 GPa as a function of porosity (0.34 to 0.52) and binder content. To put this in perspective, the Youngs modulus of the glass material particles was 64 GPa and while that of unbounded glass agglomerates was estimated to be 0.002 GPa. Thus, the ratio between the Young's modulus of the bounded particles to that of the Young's modulus of the particles was approximately 0.006-0.03 to 0.08. The dependence of Young's modulus of bounded glass particles on porosity was approximately found to be given by an exponential expression:

$E(g_a) = E_0 exp(-A\, g_a)$.

Banerjee and Adams (2003) used finite element analysis (FEA) to obtain Young's modulus of polydisperse (wide range of particle size distribution) polymer bounded explosives (PBX). Banerjee and Adams (2003) found that the results for the Young's modulus obtained with the differential effective medium approximation (DEMA) of and FEA are relatively close.

To be inclusive, the data on the stiffness of unbound packed powder beds was also reviewed. Yanagida et al. (2002) presented data for the characterization of the stiffness of "loosely" packed beds of glass and sand using a vibration-based method. The data indicates a dependence of $(g_a)^4 D^{-1/3}$, where D is the particle diameter, although the size of the particle used was very large.

Binder effect on the elastic properties of the coating

For our application, the binder (PVDF) is soluble in the solvent (NMP). At the solubility point, the binder precipitates out of the solution and becomes part of the solid phase. As for the electrode, the binder keeps particles in contact when they are locally subjected to tensile stresses. It is thus considered here, that the binder properties would govern the elastic properties of the coating when in tension while the solid particles and binder would both affect the elastic properties in compression. Thus, the coating is expected to have different elastic properties in tension and compression.

Particle packing and solvent capillary effects

Another factor that affects the state of stress in the coating is the particle packing in the coating. Particle packing occurs as a result of solvent loss through evaporation. The coherency point is defined as the instant when there is enough contact among particles such that the network of particles connected through binder ligaments can support stresses, $g_{s,c}$. In other terminologies, the coherency point is referred to as percolation point. Before the coherency point would be reached, the coating surface is mainly covered with solvent and capillary forces are not present. After the coherency point is reached, the meniscus starts to form between particles on the coating surface, and surface tension

effects start to affect the particle redistribution in the coating. The solid fraction would increase after the coherency point to its final value, $g_{s,f}$.

The capillary effects would affect the particle rearrangement between the coherency and final packing point, i.e., $g_{s,c} < g_s < g_{s,f}$. After the final packing point was reached until the end of evaporation, the porosity – or air fraction – starts to increase as the solvent fraction decreases, i.e., $g_s = g_{s,f}$ and $g_a < 1-g_{s,f}$. the solvent meniscus, which follows the drying front, is located within the coating. The solvent flow to the drying front occurs through the inter-particle space, whose permeability would vary with the solid fraction, and the liquid pressure effects on the coating particles must be considered.

Elastic properties of non-homogeneous media

There are a large number of correlations that were developed to estimate the Young's modulus of porous media or packed beds, in general. Kaczmarek and Marc (2006) reviewed the relationships for continuous solid skeleton, excluding granular loose media, grouping them in six categories: (1) empirical models (linear, exponential, power, and fractional relationships) (2) averaging or mixture rules, (3) micromechanical models, (4) minimum solid area models, (5) numerical simulation models, and (6) critical porosity and percolation models. Most of these models were developed for other applications than film drying, such as powder metallurgy, die compaction, sintering (Wang, 1984).

McCartney and Kelly (2008) presented relationships based on Maxwell's averaging methodology for dilute mixtures for obtaining Young's modulus, bulk modulus K_{eff}, shear modulus (G), and thermal expansion of the in-homogeneous media, α_{eff}. These averaging relationships can be cast as:

$$\frac{1}{q_{eff}+w} = \sum_{i=1}^{N} \frac{g_i}{q_i+w}$$

where q indicates the property to be averaged (K, G) and w indicates the averaging weight $\left(\frac{4G_m}{3}, \frac{9K_m+8G_m}{6(K_m+2G_m)}G_m\right)$,

where subscript "m" indicates the matrix material. The effective thermal expansion coefficient, α_{eff}, is given as:

$$\frac{\alpha_{eff}}{1/K_{eff}+1/w} = \sum_{i=1}^{N} \frac{g_i\alpha_i}{1/K_i+1/w}$$

with $w = \frac{4G_m}{3}$. These averaging expressions were derived with the consideration that the stress state in each of the spherical particles does not depend on the stress state in the other particles.

Stress-strain formulations for coating drying

Several approaches were found on the stress-strain formulations for coating drying. Overall, three main approaches were found. The first approach considered is the bi-axial formulation. For film coating over large areas, which is the case for this project, the state of stress can be assumed to be bi-axial. Considering z to denote the axis normal to the web surface, the strains and stresses are identical in the x and y axes respectively ($\varepsilon_{xx} = \varepsilon_{yy}$ and $\sigma_{xx} = \sigma_{yy}$). There is wealth of literature on the bi-axial state of stress of thin films. It is worth noting that the well-known Stoney formula, which is derived for a bilayer strip in which the film thickness is much smaller than the substrate thickness (Stoney, 1909), cannot be applied here, as the web thickness is comparable to that of the coating. Hsueh (2002) gives analytical expressions for the stress and strains for a multiple layers due to

different thermal expansion property of the layers. However, drying is not considered.

The second approach is based on the one-dimensional compaction theory developed by Routh and Russel (1999) for the study of latex film formation. Routh and Russel (1999) approach was based on the deformation of a pair of particles due to both interfacial tension and external forces exerted by contacting neighbors, followed by the volume averaging over all possible orientations of the pair to obtain a macroscopic stress-strain formulation. One of the main assumption in the Routh-Russel model is that the strain is non-zero only in the direction normal to the surface, i.e., $\varepsilon_{ij} = \varepsilon\delta_{3i}\delta_{3j}$. Routh-Russel model was used by Tirumkudulu and Russel (2004) for both polymeric, viscoelastic particles, and for elastic particles in a simplified form. It is interesting to note that in the same paper, experimental data is presented for the stress in the film using the Stoney formula (for which $\varepsilon_{xx} = \varepsilon_{yy} \neq 0$) while the analytical formulation for stress analysis is based on Routh-Russel model (for which $\varepsilon_{xx} = \varepsilon_{yy} = 0$). Moreover, the stress-strain equations in Tirumkudulu and Russel (2005) are slightly different than those in Tirumkudulu and Russel (2004), most probably due to a typo.

The third approach is based on poroelasticity theory, which is a field by itself evolving from dealing with rock mechanics, soil mechanics, food industry, wood industry, and polymer science (Biot, 1941; Rice and Cleary, 1976). Relatively recently with respect to the time scale of the poroelasticity literature, Scherer in a series of articles (Scherer 1986, 1989, 1990) developed constitutive equations for drying by employing several assumptions to simplify the poroelasticity equations. Scherer included the capillary-flow effects on the drying stress by assuming: Compressible and (visco)elastic solid matrix, constant evaporation rate in the first drying stage (when the capillary forces at the drying surface rise), constant permeability, saturated solid matrix, and incompressible solid. Recently, Puyate and Lawrence (2009) pointed out that Scherer's approach is not accurate at slow drying rates and that the compressibility of the solid matrix, which was neglected by Scherer, may play an important role. Puyate and Lawrence (2009) developed a pressure diffusion-like equation by taking into account compressibility of the solid matrix and extending its applicability to the drying regime in which the drying front recedes in the coating. It has to be noted that all the analytical expressions derived by Scherer and Puyate and Lawrence (2009), including a pressure diffusion equation using Darcy's law, are for isothermal drying of a film on a rigid substrate without considering the thermal expansion in the coating and/or substrate. The main concepts and advances that were relevant for the stress analysis of coating drying are reviewed in Table 9.

Table 9. Main features needed for the stress analysis during drying of coatings on flexible multiple layered substrates

Approaches	Drying	Multi-layer	Thermal expansion	Flexible substrate	Capillary forces	Receding front	Particle packing
Bi-axial multilayer	-	Y	Y	Y	-	-	-
1D compaction	Y	-	-	-	-	Y	Y
Poroelasticity	-	Y	-	Y	Y	-	-
Scherer	Y	-	-	-	Y	-	-
PL09	Y	-	-	-	Y	Y	-
This study	Y	Y	Y	Y	Y	Y	Y

Stress-strain formulations for coating drying on flexible substrates considering capillary forces

New constitutive equations were developed in this study in order to complete the model development. In the system considered, the coating is considered to be material of index 1, with the other substrate materials labeled in increasing order from the coating down. The stress within an elastic isotropic material is given by:

$$\sigma_{ij} = -\frac{E}{1+\nu}\left(\varepsilon_{ij} + \frac{\nu}{1-2\nu}\varepsilon_V \delta_{ij}\right) - \frac{E}{1-2\nu}\varepsilon_{th}\delta_{ij} \quad (1)$$

where E is Young's modulus, ν the Poisson's ratio, and ε_V is the volumetric strain ($\varepsilon_V = \varepsilon_{ii}$). The stress within a saturated, porous, and isotropic elastic materials is given, as (Puyate and Lawrence, 2009; Suvorov and Selvadurai, 2011):

$$\sigma_{ij} = -\delta_{ij}P_L + \frac{E_{ps}}{1+\nu_{ps}}\left(\varepsilon_{ij} + \frac{\nu_{ps}}{1-2\nu_{ps}}\varepsilon_V \delta_{ij}\right) - \frac{E_{ps}}{1-2\nu_{ps}}\varepsilon_{th}\delta_{ij} \quad (2)$$

where the subscript "ps" indicates properties of the porous solid matrix (not those of the solid itself) and $P_L = p_L - p_{atm}$ is the gauge pressure in the liquid.

Due to the lack of mechanical loading and the small thickness of the coating and web substrate, the assumption of a bi-axial state of strain/stress is considered to be very appropriate ($\varepsilon_{xx} = \varepsilon_{yy}$ and $\sigma_{xx} = \sigma_{yy}$). Also, following the derivation presented in Puyate and Lawrence (2009), for the stress in the normal direction, σ_{zz}, it can be shown that $\sigma_{zz} = 0$ in all the layers in the system considered. Following the derivation for the multilayer films, the strain in the substrate layers can be decomposed into a uniform component, ε_o, and a bending component, without explicitly considering the position of the neutral axis, as:

$$\varepsilon = \varepsilon_{xx}|_k = \varepsilon_o + \varrho\, z \quad (3)$$

where ϱ is the reciprocal of the curvature.

Thus, it can be shown that the relationships between the in-plane stress, $\sigma_k = \sigma_{xx}|_k$, and in plane strain, $\varepsilon_k = \varepsilon_{xx}|_k$, for a layer of index k, are given for the coating as:

$$\sigma_1(\varepsilon, P_L) = E_1'\left(\varepsilon - \varepsilon_{th,1}\right) - c_1 P_L \quad (4)$$

and for the substrate layers, as:

$$\sigma_k(\varepsilon) = E_k'\left(\varepsilon - \varepsilon_{th,k}\right)$$

where $E_k' = \frac{E_k}{1-\nu_k}$ is the bi-axial Young's modulus and c_1 is a constant that depends on the Poisson's ratio. For the coating, the Young's modulus and the Poisson's ratio are those of the porous solid matrix as indicated in equation (2). From the stress-strain relationship for the normal stress, $\sigma_{zz} = 0$, the following relationship, which is referred to as the pressure-strain equation (PSE), can be obtained between P_L and ε_V:

$$\frac{P_L}{E_1} = c_2\varepsilon_V - c_3\varepsilon_{th,1} - c_4\varepsilon \quad (5)$$

where c2, c3, and c4 are constants that depend only on the Poisson's ratio. Another equation, which is termed "void occupancy equation" – to use the poroelasticity terminology – describes the change of the mass of fluid, Δm_L, in the interparticle space with respect to the initial mass of the fluid, m_L, as (Rice and Cleary, 1976; Suvorov and Selvadurai, 2011):

$$-g_L\frac{\Delta m_L}{m_L} + \alpha_B\varepsilon_V + \left(\frac{g_L}{K_L} + \frac{\alpha_B - g_L}{K_S}\right)P_L = 3\varepsilon_{th,SL} \quad (6)$$

where $\varepsilon_{th,SL}$ is an equivalent thermal expansion strain of the coating (including the solvent, binder, and solid particles), K_L is the bulk modulus of the liquid phase, K_S is the bulk modulus of the solid phase, $\alpha_B = 1 - \frac{K_{ps}}{K_S}$ is the Biot parameter, which depends on the bulk modulus of the porous solid (drained condition) and that of the solid phase itself. Combining Darcy's law, which relates the fluid velocity to the pressure gradient, and eigenstrain due to the change in fluid mass, $\frac{\Delta m_L}{m_L}$, to the divergence of the fluid velocity, the following relationship can be written:

$$g_L \frac{\Delta m_L}{m_L} = \int_0^t \frac{\partial}{\partial z}\left(\frac{k_{D,L}}{\mu}\frac{\partial P_L}{\partial z}\right) dt \tag{7}$$

and the "void occupancy equation" (VOE), after taking the time derivative, becomes:

$$\alpha_B \dot{\varepsilon}_V + \left(\frac{g_L}{K_L} + \frac{\alpha_B - g_L}{K_S}\right)\dot{P}_L - \frac{k_{D,L}}{\mu}\frac{\partial^2 P_L}{\partial z^2} = 3\dot{\varepsilon}_{th,SL} \tag{8}$$

As it can be seen, the pressure-strain equation (5) can be combined with the void occupancy equation (8) to eliminate ε_V and obtain one master equation for the pressure, P_L.

Aside from ε_V and P_L the other unknowns are ε_o and ϱ. Thus, two additional equations are needed to complete the systems of equations. These additional equations are force balance and momentum balance equations for the entire multilayer system, as they are traditionally considered for bi-axial stressed films. The formulation of the force balance equations is not trivial for a drying coating since one force balance is usually written for the uniform strain component and another one for the bending strain component. In this study it is considered that the force component from the stress due to the liquid pressure contributes to the force balance for the uniform strain component. The resultant force balance and momentum balance are given as:

$$\int_{z_2}^{z_1} \sigma_1\,(\varepsilon_o, P_L)dz + \sum_{k=2}^{N}\int_{z_{k+1}}^{z_k} \sigma_k\,(\varepsilon_o)\,dz + \sum_{k=1}^{N}\int_{z_{k+1}}^{z_k} E'_k\,\varrho\,z\,dz = 0, \tag{13}$$

$$\sum_{k=1}^{N}\int_{z_{k+1}}^{z_k} \sigma_k\,z\,dz = 0. \tag{14}$$

Since ε_o and ρ are constant with respect to the "z" coordinate, equations 13 and 14 can be integrated, as:

$$\varepsilon_o \sum_{k=1}^{N} E'_k \int_{z_{k+1}}^{z_k} dz + \varrho \sum_{k=1}^{N} E'_k \int_{z_{k+1}}^{z_k} z\,dz \; - \frac{1-2\nu_1}{1-\nu_1}\int_{z_2}^{z_1} P_L\,dz = \sum_{k=1}^{N} \varepsilon_{th,k} E'_k \int_{z_{k+1}}^{z_k} dz, \tag{15}$$

$$\varepsilon_o \sum_{k=1}^{N} E'_k \int_{z_{k+1}}^{z_k} z\,dz + \varrho \sum_{k=1}^{N} E'_k \int_{z_{k+1}}^{z_k} z^2 dz \; - \frac{1-2\nu_1}{1-\nu_1}\int_{z_2}^{z_1} P_L\,z\,dz = \sum_{k=1}^{N} \varepsilon_{th,k} E'_k \int_{z_{k+1}}^{z_k} z\,dz, \tag{16}$$

Denoting $A_{N,k} = E'_k \int_{z_{k+1}}^{z_k} z^N dz$, the two relationships can be written as:

$$\varepsilon_o \sum_{k=1}^{N} A_{0,k} + \varrho \sum_{k=1}^{N} A_{1,k} \; - \frac{1-2\nu_1}{1-\nu_1}\int_{z_2}^{z_1} P_L\,dz = \sum_{k=1}^{N} \varepsilon_{th,k}\,A_{0,k}, \tag{17}$$

$$\varepsilon_o \sum_{k=1}^{N} A_{1,k} + \varrho \sum_{k=1}^{N} A_{2,k} \; - \frac{1-2\nu_1}{1-\nu_1}\int_{z_2}^{z_1} P_L\,z\,dz = \sum_{k=1}^{N} \varepsilon_{th,k}\,A_{1,k}, \tag{18}$$

Thus, using the following notations, $a_{11} = \sum_{k=1}^{N} A_{0,k}$, $a_{12} = \sum_{k=1}^{N} A_{1,k}$, $a_{22} = \sum_{k=1}^{N} A_{2,k}$, $a_{13} = \frac{1-2\nu_1}{1-\nu_1}$, $b_1 = \sum_{k=1}^{N} \varepsilon_{th,k}\,A_{0,k}$, $b_2 = \sum_{k=1}^{N} \varepsilon_{th,k}\,A_{1,k}$, the resulting equations for ε_o and ρ can be cast in the following form, respectively:

$$\begin{cases} a_{11}\varepsilon_o + a_{12}\rho - a_{13}\int_{z_2}^{z_1} P_L dz = b_1 \\ a_{12}\varepsilon_o + a_{22}\rho - a_{13}\int_{z_2}^{z_1} z P_L dz = b_2 \end{cases} \tag{19}$$

Cracking of coatings

There are numerous studies on the vast topic of cracking criteria of dried coatings and an extensive review is beyond the scope of this report. In this section, a few concepts and considerations that can be used for the development of cracking criteria are highlighted. Two concepts are reviewed here that can be used to assess the cracking tendency of coatings. One property that is relevant to the coating damage is the tensile strength of the solid matrix, which must include the effect of the binder. Another one is based on linear elastic fracture mechanics.

First, one property that is relevant to the coating damage is the tensile strength of the solid matrix, which must include the effect of the binder. For temperatures less than 100 ^{o}C, Hellinckx and Bauwens (1995) reported that the yield strength of PVDF can be given as a function of the temperature and strain rate. To be concise, some data shown by Hellinckx and Bauwens (1995) on the yield strength of PVDF is shown in Table 10. It is expected that for particulate coatings using PVDF as binder, the effective yield strength would be smaller than that for bulk PVDF. In this study, we propose that, without knowing the exact amount of PVDF that plays an active role in binding the particles, the effective yield strength due to the binder be scaled with the amount of PVDF, as $\sigma_{y,coat} = g_b \sigma_{y,b}$, where g_b is the binder fraction in the coating and $\sigma_{y,b}$ is the yield stress of the bulk binder.

Another consideration is the strain level that can be sustained by the binder. From the stress-strain experimental data of carbon black filled PVDF, which were conducted at room temperature, it was found that the PVDF films with 10 and 25 pph of carbon black can only be stretched to about 4% before breaking (Chen et al., 2003).

The yield stress of the dried silica coatings, σ_y, was estimated using a semi-empirical relationship to be 33 to 58MPa (Di Giuseppe et al., 2012). Compared to the wet gels data from Zarzycki (1988), Young's modulus exhibited a value larger by 100 times (dried). Di Giuseppe et al. (2012) measured the rheological and mechanical properties using shear rate tests, oscillatory methods, indentation and an ultrasonic technique at solid fractions of 0.35 to 0.6 of aqueous mono-disperse silica suspensions. It is worth mentioning that concerning the mechanical behavior, the shear thinning was observed for solid fractions of 0.35 to 0.5, with the elastic solid domain starting at solid fractions of 0.51.

Table 10. Yield strength [MPa] of PVDF at different temperatures and strain rates

Temperature [^{o}C]	0	25	50	75	100	120	130	140
σ_y @ 2.1656 10^{-5} [1/s]	66	48	37	27	16	11	10	8
σ_y @ 0.19137 [1/s]	85	69	55	40	29	22	17	13

The second concept considered here is based on linear elastic fracture mechanics. Fracture mechanics theory, which describes the resistance of a material to cracking based on energy balance considerations at the crack tip, was also used for polymeric materials (Hancock et al., 1993). The elastic stress field at the crack tip is characterized by the stress intensity factor, K. The crack propagation is considered to occur when the stress intensity factor, K, reaches a critical value, K_{IC}. For dry granules of ballotini glass particles with polyvinylpyrrolidone (PVP) binder $K_{IC}(g_S) = K_{IC,o} exp\left(-B\ (1 - g_S)\right)$, where $K_{IC,o}$=35.7772 and B=-12.4822 for porosity fractions between 0.35 to 0.6. From these considerations (Hancock et al., 1993; and Brown and Yang, 1990), for a film of thickness h, that experiences a stress, σ, the cracking criterion is:

$$h \geq 0.884 \left(\frac{K_{IC}(g_S)}{\sigma}\right)^2$$

It appears that the only study on wet gels that provides data on critical stress intensity factors is that of Zarzycki (1988). The K_{IC} for wet Ludox silica gels, at solid fractions of 23%, was measured to be between 1 to $2x10^{-4}$ MPa $m^{1/2}$ while the biaxial modulus of the coating varied between 0.02 to 2 MPa.

Scherer (1990) discussed two cracking mechanisms and concluded that in the context of fracture mechanics framework, the cracking is likely to be caused by the macroscopic stresses that act on the flaws that are induced by an irregular drying front. Advancing the discussion on stresses in drying bodies, Scherer (1992) indicated that the stress in the solid network, $\sigma_{s,xx} = \sigma_{xx} - g_L P_L$, could be tensile. To be inclusive, the stress in the solid network could cause a fracture in the solid network elements (particles, filaments) provided that the stress intensity factors for the solid phase are reached for flaw sizes in the solid phase elements.

Results for the coating properties

The Young's modulus, Poisson's ratio and the coefficient of thermal expansion are required for the stress analysis. The properties of different constituent materials for the various layers of the web are shown in Table 11. In order to estimate these mechanical properties, properties for the anode and coating, it was assumed that the anode layer is composed of 92% mesophase carbon microbeads (MCMB), 4% polyvinylidene fluoride (PVDF) and 4% carbon conductive. The dried coating was composed of 65% silica particles and 35% PVDF.

Table 11. Properties of different constituent materials used in the analysis

Material	MCMB Carbon conductive	PVDF	Silica	Copper
Elastic Modulus [GPa]	10	2	71	110.3
Poisson's ratio	0.3	0.34	0.17	0.347
Coefficient of thermal expansion [$\times 10^{-6}$ /°C]	6.6	200	0.55	16.6
Density [g/cm^3]	2.25	1.75	2.65	8.94

Data it is presented here for the Young's modulus within the NCS coating. Various formulations have been used to obtain the Young's modulus in the compressive and tensile state. In Figure 32, the following data is presented:

(a) $E_{compr,\ sol}$ – Young's modulus obtained using Maxwell averaging with solvent as the matrix,

(b) $E_{compr,\ part}$ – Young's modulus obtained using Maxwell averaging with solid particles as the matrix,

(c) E_{tens} – Young's modulus in tension state. This modulus is limited by the binder Young's modulus as $E_{tens} = E_{binder} * g_{binder}$, where g_{binder} indicates the volumetric fraction of the binder

(d) $E_{part+binder}$ – Young's modulus of the solid matrix material, i.e., considering only the particles and the binder.

The final Young's modulus, $E_{compr,\ expon,}$ was obtained by considering that between the percolation point (taken here at 47% solid loading) and saturation point (taken here 80% solid loading), the Young's modulus varies based on an exponential relationship as a function of interparticle void

fraction $E(g_S) = E_0 exp\left(-A\ (1 - g_S)\right)$ (as shown in previous sections based on experimental data by Hancock et al., 1993).

In Figure 33, this data is shown for two cases. In one case, the Young's modulus was not prescribed any upper limit, as given by the Maxwell averaging formula. On the other hand, as discussed in the previous sections, the experimental data by Hancock et al., 1993 suggests that the predictions of the Young's modulus are somehow limited by the binder properties, thus in the second case – lower line in the figure, it was considered that the maximum Young's modulus in compression is limited by 4* E_{binder}.

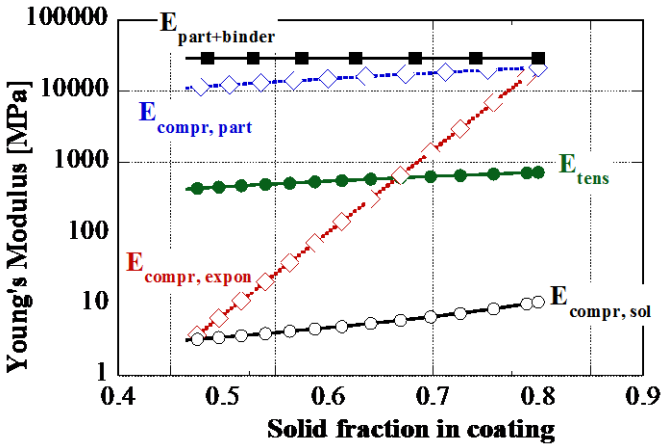

Figure 32. Young's modulus estimations using different formulations.

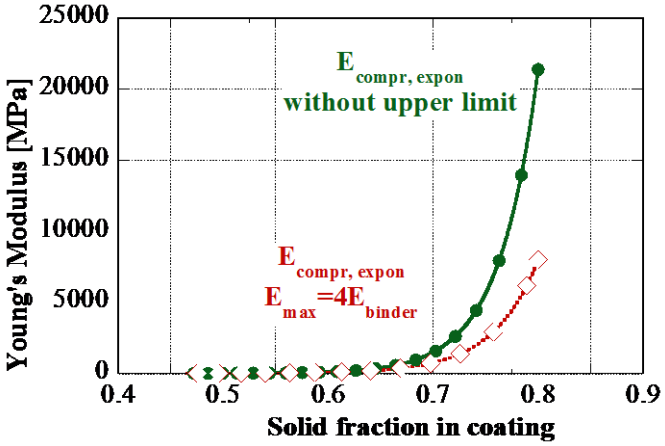

Figure 33. Young's modulus as a function of solid fraction in the coating. Upper line represents the data without any upper limit, i.e., just using the Maxwell averaging. Lower line represents the data that includes an upper limit for the Young's modulus.

Results for the stress within the coating

The data in the Figure 34 show the results for a stress analysis obtained after coherency was reached in the coating. For these results, it was also considered that liquid menisci start to form at the top surface of the coating. Thus, the coating is also subject to the capillary pressure from the top surface.

The simulation for the data presented here was ended when the liquid front is expected to recede into the coating, i.e., when the pressure in the solvent at the top surface reached the capillary pressure. After the liquid front starts to recede in the coating, the stresses in the coating are likely to exhibit lower values than those when capillary forces are present (Scherer, 1992). The results presented in Figure 33, show that tensile stresses in the coating are possible. These tensile stresses are likely responsible for the cracking of coatings.

4.3 PROCESS DEVELOPMENT

4.3.1 Coating Development

The ultimate goal of this task was to develop a coating process which deposits nanocomposite layers on any substrate without cracking and with good adhesion at economically viable rates. This has been achieved for target thicknesses at rates equaling those of our commercial coating lines.

While the study focus is drying, slurry quality parameters and equipment optimization supersede drying issues and so must also be included in the analysis (Table 12).

Table 12. Slurry equipment parameters

VARIABLE	IMPACT	SOLUTION	COMMENT
Slurry agglomerates	Agglomerates > ~3-5µ cause cracking via stress concentrating.	Filter the solution	Figure 34. Filtering is routine; additionally, the slurry should be well mixed prior to filtering.
Temporal viscosity stability	Slurry viscosity drift during the run can lead to clumps and bubbles.	Extended mixing provides excellent temporal stability.	Figure 35.
Appropriate Viscosity	Meets target for the thickness	Adjust % solids	Figure 36. A range of viscosities were developed for coating line optimization
Coater optimization	Speed and gap	Optimize the coating gap and slot height relative to substrate	Figure 37. Gap to substrate distance and proper shimming are eliminate trapped air & thickness nonuniformities.
Bubble - Trapped Air	Trapped bubbles concentrate stress and create cracks	Degas the slurry	In addition degassing, lines need to be tight so that no further air ingress occurs during pumping.

The process development focused on three optimization parameters: optimum agglomerate size, minimizing mixing time, and coating line optimization.

Agglomerates; Improved slurry filtering and degassing eliminated this issue at the A123 Boston pilot facility: a 200-300 um filter to remove the big chunks which are characteristically dust and/or gels, and protects the finer filter from clogging excessively follow by a second 50 micron filter.

Mixing time: This variable impacts crack development as shown below in Figure 34. At low mixing time there are agglomerates; crack density is highest after ten minutes after which it then decreases again. After 24 minutes the cracks have disappeared but the surface is still rough; 44 minutes was

sufficient to eliminate cracks and to smooth out the surface and is the standard now.

Coating line Optimization. Figure 37. Variables of slurry rheology, back pressure and distance between the die and the roll inter-relate and optimization requires adjustment of all. The gap variable is especially critical for laying down a uniform coating without entrapping additional air. The slurry has a naturally high viscosity at low shear which is good for quickly setting the coating once deposited on the substrate.

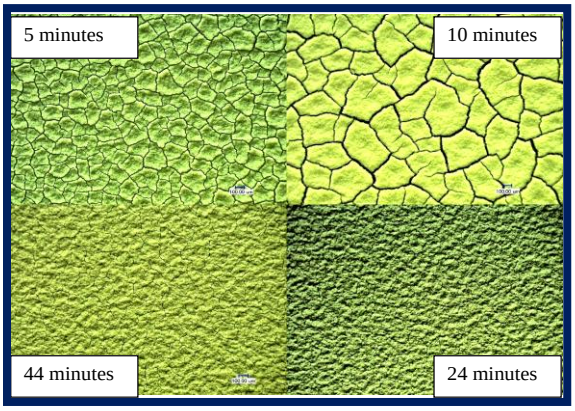

Figure 34. 100X image comparing surfaces from slurries of different mixing times.

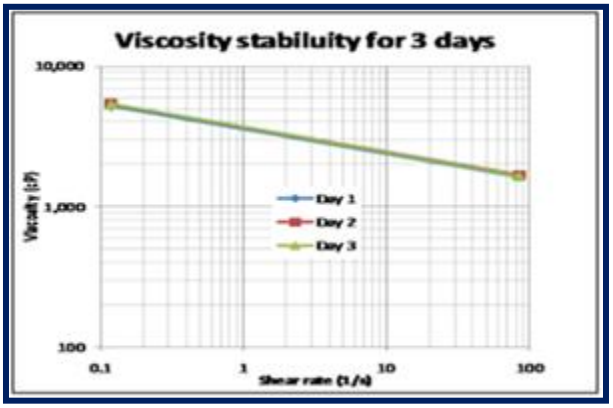

Figure 35. Slurry mixed at >40 minutes has excellent stability over three days.

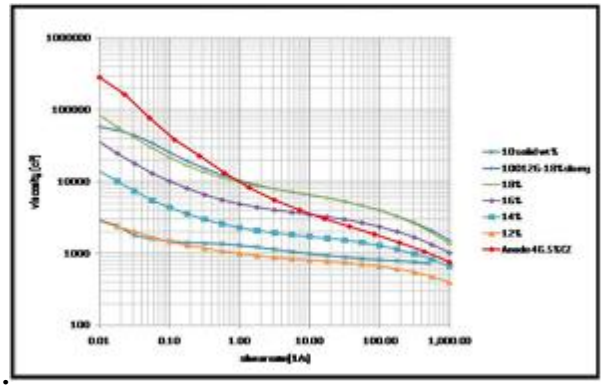

Figure 36. Slurries of range of solids, up to 1.8X the original, were developed which have the appropriate target viscosities.

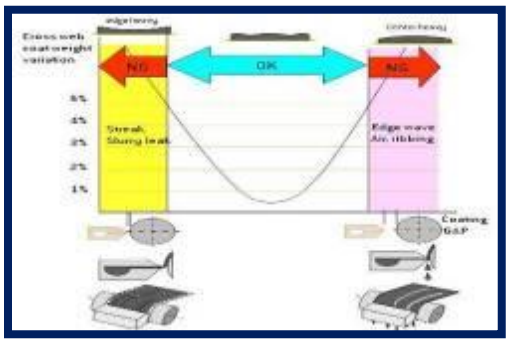

Figure 37. Appropriate gap positioning eliminates gas trapping/bubble formation, which can lead to cracks. Web thickness uniformity eliminates variations which can result in cracking.

While the program progressed it was discovered that the above described parameters are also critical. Once these were optimized, cracking issues were significantly reduced and were found to occur only when nanocomposite coatings were dried very quickly and were greater than 10-15um thick. The final variable which enabled routine high quality crack-free coatings is the time between laying the slurry on the substrate and initiation of drying; it was found that the slurry viscosity needed to increase very quickly once it was laid down so that there is no flow. This could be realized only with IR drying within approximately 10 seconds from lay-down. Overhead drying with convective heat dries the surface, not the bulk, and so does not change the viscosity of the bulk. Figure 38 shows a typical coating which has no cracks and excellent thickness uniformity.

a)

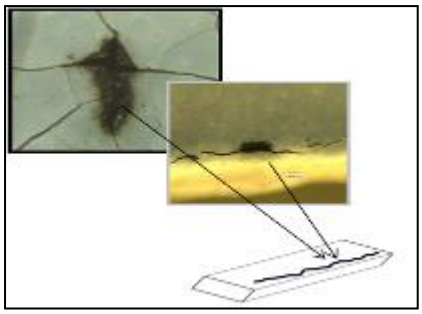

b)

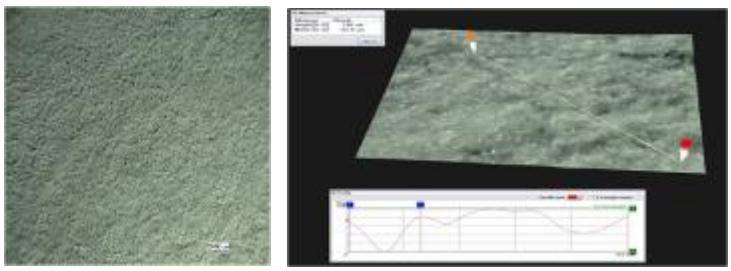

Figure 38. A – initial cracking with optimized slurry and equipment results in cracking at high stress points – such as the edges, B – surface at 100X and optical surface profile showing that nonuniformities of +/- 1.2um were obtained once IR heating was implemented.

4.3.2 Critical Thickness Determination and Drying Study

The goal of this task was to develop a coating process which deposits nanocomposite layers on any substrate without cracking and with good adhesion at economically viable rates. A coating process was optimized during the scope of this project by A123 in which target thicknesses were achieved at rates equaling those of typical commercial coating lines. The optimization included the refining of slurry quality parameters and equipment optimization. The hypothesis at the start of the program was that drying issues dominated coating quality, and, as the program progressed, it was discovered that slurry quality parameters and equipment optimization superseded the drying issues. Once the variables of slurry agglomerates, temporal viscosity stability and viscosity control, slot die coating gap and speeds, and entrapped air bubbles, drying stresses during and immediately after coating were studied.

As stated previously, one way to reduce costs for battery fabrication is by changing the coating speed. Coating process variables greatly control the speed at which a coating can be processed without drying cracks. As these variables were addressed by A123, ORNL began examining the effects of process variables from the drying side. Certain variables such as coating speed, temperature ranges, and environmental conditions (IR versus radiant heat) were defined by the A123 coating production profile, but variations upon these conditions were examined to better understand and define the stress development during coating drying.

Understanding the stress development during coating drying is an important step in understanding the processing-property relationship between these defined variables. Unfortunately, stress in a supported coated material cannot be measured directly. The measurement of stress during drying is typically inferred from other properties, such as deflection, or visually evidenced from flaw initiation and propagation, such as a crack. As a result, the ability to study the mechanism of cracking evolution during coating drying was the major focus during this project. One of the goals was to develop an in-situ drying technique that could examine the effects of the A123 drying variables on stress/cracking evolution in the nanocomposite separator layer. Initially, the in-situ method to study drying evolution used an optical microscope on drawn down as-cast coatings. As the technique and the study refined, drying was examined during coating where the microscope could be mounted directly onto the coating system. Nanocomposite coatings were cast on a variety of substrates including the A123 anode and cathode, glass slides, silicon wafers, and a ceramic substrate. The substrates were varied to examine the effects of substrate surface roughness and slurry-substrate wetting upon the coating efficacy. Coating thickness was varied in order to determine the critical thickness, i.e., the thickness at which drying cracks are initiated, during IR and/or radiant heat drying due to wetting variations and determine the root cause of any drying defects if they occurred. Composite thicknesses were determined for three composite coating compositions with the five substrates. The thickest coating achievable was 10 mils on a relatively smooth, high surface energy surface for all the coating compositions, while the thinnest critical thickness was 3 mils on the model substrate of silicon, again, for all coating compositions. The role of the substrate in the coating drying and efficacy was thus demonstrated.

As the technique progressed, critical coating thicknesses as well as evaporation rates of the solvent system under infrared heating was generated. The experimental data was provided to the drying task, and the subsequent model developed in that task. Figure 39 graphically depicts the coating structure as a function of thickness during drying. The on-set of cracking and crack propagation is visually evident from this series of images.

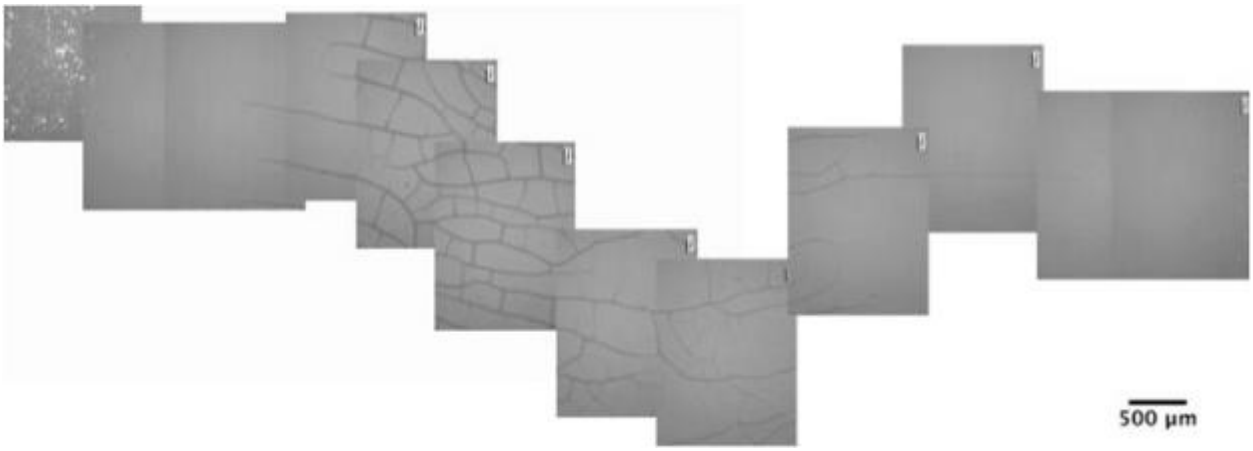

Figure 39. Micrographical series of dried coating with determination of on-set cracking and critical thickness

Figure 40 shows the thickness of the coating across the width. The large variation in thickness is intentionally prepared in order to determine the critical thickness with a minimum of experimental expenditures.

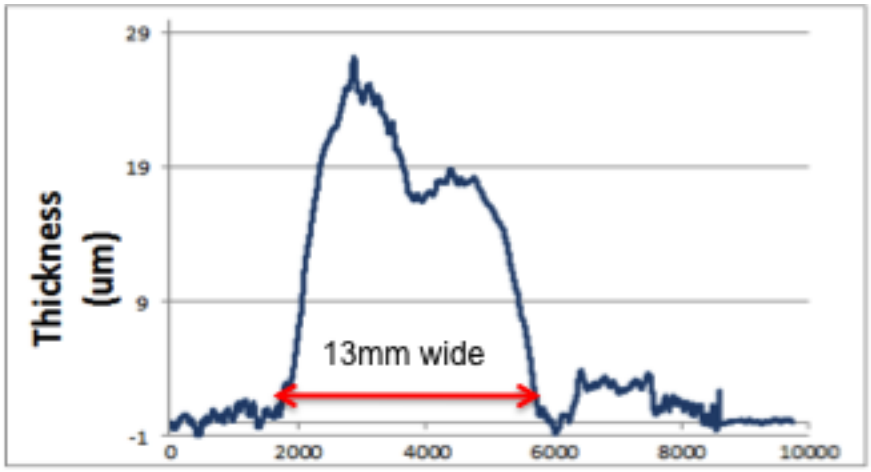

Figure 40. Thickness across the width of a coating.

4.3.3 Design Evaluation of High Speed Web Handling System

ORNL worked with equipment manufacturers to design and deliver a high speed web handling system. In a competitive procurement process, such a system has been quoted, designed and manufactured for demonstration at Oak Ridge National Laboratory. The final system can be seen in figure 41.

The system is able to handle a variety of webs including coated and non-coated current collector foils at the following metrics.

Line Speed (Max.): 400 ft./min. (122 m/min.)

- Line Speed (Min.): 20 ft./min. (12.2 m/min.)
- Web Width (Max.): 12 in. (300mm)
- Web Width (Min.): 2 in. (50mm)
- Coating Widths: 2”, 6”, 8”, 10”
- Tension (Max.): 30 lbf
- Tension (Min.): 5 lbf
- Roll O.D. (Max.): 14 in.
- Core I.D. (Nom.): 3 in.
- Roll Weight (Max.): 250 lb. (112.5kg)
- Coatings UV coatings
- Coat Weights: TBD
- Solvents 100% solids typical with occasional trace solvents
- Machine Dimensions: 76.25”(L) x 50.75”(W) x 89.7”(H with UV lamps)
- Space at Buyer’s facility: 144” (L) x 108” (W) x 108” (H)

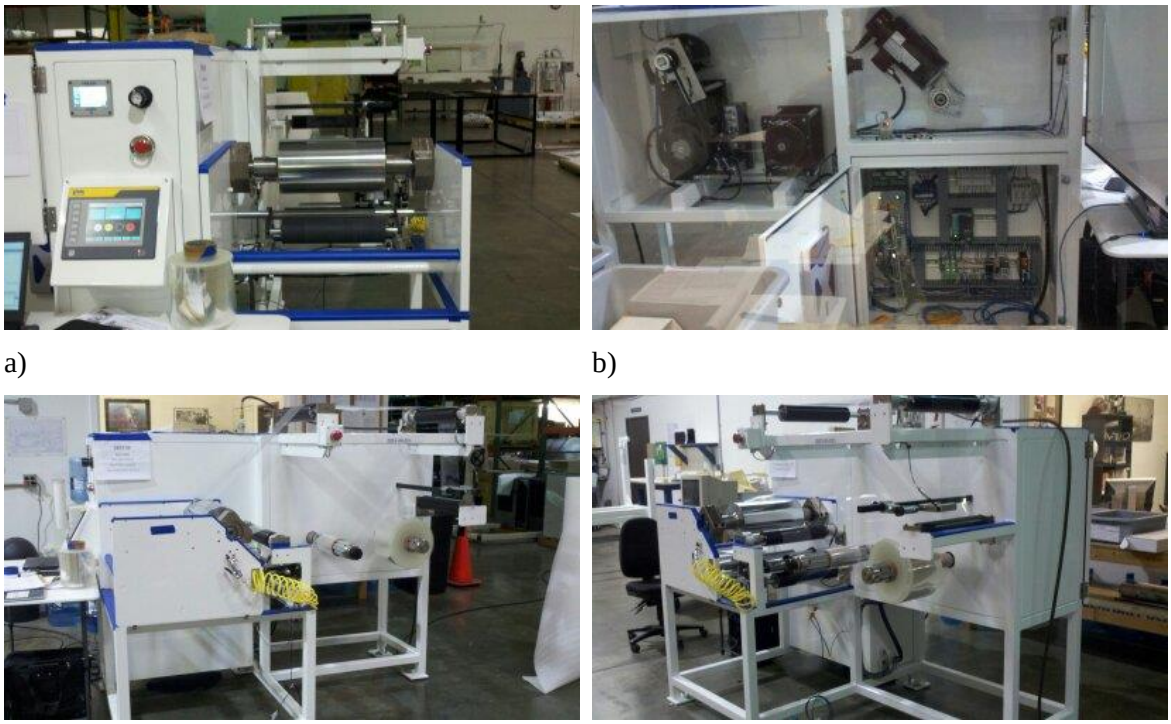

a) b)

c) d)

Figure 41. High speed web handling system manufactured by Conquip, CA with full tension control, speed control, unwind and rewind. Treatment options can be added at several locations.

4.4 DEVELOPMENT OF QUALITY CONTROL AND SAFETY TESTING

4.4.1 Online Quality Control

This research and development initiative was focused on the development of hardware and methods for online dielectric breakdown tests. These efforts were specifically directed toward development of test methodologies for measuring the dielectric breakdown of lithium-ion battery electrodes with nano-composite dielectric coatings. The research efforts focused on the use of a highly specialized custom electrode adapted to the manufacturing processes for these materials.

An 8" x 12" granite surface plate was chosen for the test surface to provide a very stable platform onto which the specimens could be mounted for testing. An adhesive aluminum electrode was placed on the granite surface plate to provide the low-voltage contact with the specimen. A current sense resistor was placed in series with that electrode and connected to ground potential. This resistor provided the means for obtaining a current signal. An oscilloscope was used in the initial tests to monitor the current signal. A high-voltage laboratory power supply was connected to the custom electrode, which was placed in contact with the test specimen (Figure 42).

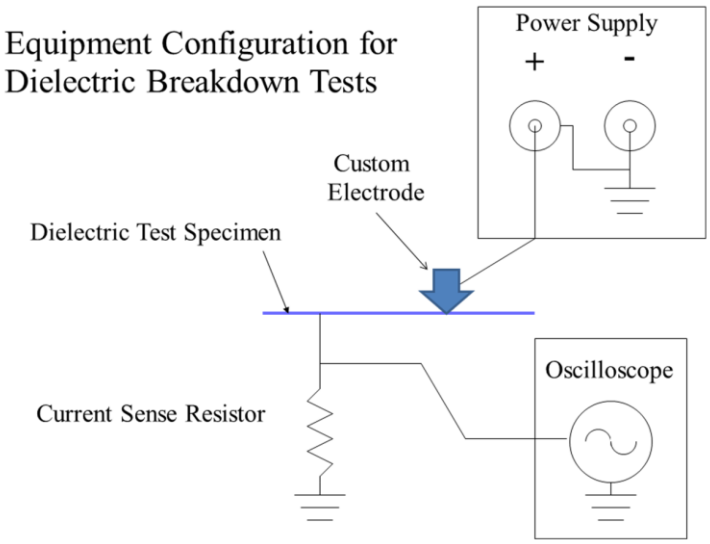

Figure 42. Initial experimental setup.

In the initial tests, which were conducted in ambient air conditions, the electrode was manually translated over the surface of the test specimen as the current signal was monitored on the oscilloscope. Fairly substantial leakage currents were observed during these tests, along with some identifiable dielectric breakdown events. It was quickly determined that the hygroscopic nature of these coatings would require the tests to be conducted in a humidity controlled chamber, or dry box.

A rectangular desiccator box, nominally 18" x 10" x 10" was selected for the dry box. The box was modified by adding a gasketed port through which a pushrod could be attached to the custom electrode. Electrical penetrations and a port for a dry air supply line were also added. Very basic humidity strips and dial indicators were used for initial tests. The granite surface plate was installed and the box was prepared for initial tests. To facilitate automated testing a motion control system was attached to the pushrod and LabVIEW software was developed to manage the motion control as well as the signal acquisition.

Initial tests of electrode materials with this system showed a high degree of repeatability in

identifying breakdown events, which were now correlated with position as determined by the motion control system. Tests were conducted at various voltages and the breakdown events were discussed with our industrial partner. It was determined that a higher level of humidity sensing capability should be added to the chamber. A capacitive humidity sensor (Sensirion SHT75) was added to the system to enable humidity sensing down to 0% with very high resolution. Initial tests with the system showed that using a dry air purge line, the dry box could be dried from 45% ambient humidity to essentially 0% humidity in 30 minutes.

Using the dry box a variety of manufacturer-supplied samples were tested at essentially 0% humidity. Leakage currents were observed to be nil. In most cases breakdown events were limited in their occurrence, but highly repeatable when they were observed.

The initial results were promising enough that efforts were focused on applying the method toward a system in a manufacturing environment. An ORNL tape casting unit was selected for use in these efforts. Applying these tests to an actual piece of manufacturing equipment required significant modifications in terms of electrical safety and obtaining reliable results. It was quickly determined that the use of the dropping resistor for acquiring the current signal might create an electrical hazard that would be acceptable in a manufacturing environment. Consequently, it was decided that the specimen should be placed in contact with a ground potential surface. This was relatively easy to achieve with the metal frame of the tape casting unit. However, this provided no means for obtaining a current signal with the existing laboratory power supply. Consequently, a solid-state power supply (Figure 43) was selected for use in the experiment. This power supply included a current sense output terminal, an enable/disable terminal, and a voltage adjustment input terminal; all of which would facilitate the development of an intrinsically safe computer-controlled implementation of the test methodology. With these developments completed and the path to a reliable implementation and industrial environments demonstrated, the testing focus returned to laboratory experiments, which benefited greatly from the power supply and other advancements made during the development of the online implementation capabilities.

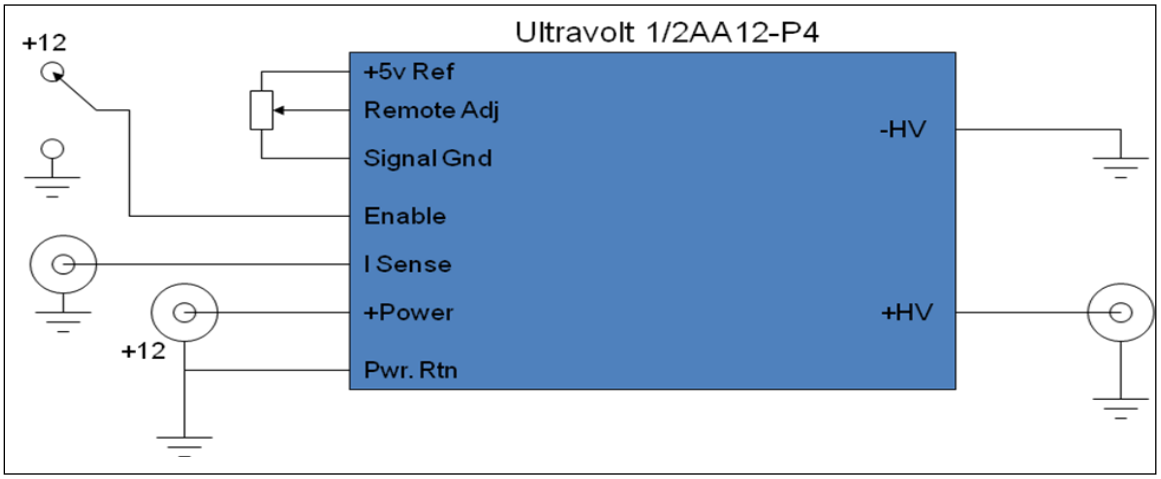

Figure 43. Solid-state power supply diagram.

The modified laboratory test equipment now included the ability to remotely adjust the voltage while monitoring the current to detect breakdown events. This facilitated the development of fully automated test software routines in which the breakdown characteristics of a sample could be automatically determined in a series of tests beginning at a very low-voltage, proceeding to a very

high-voltage in user-selectable voltage increments. The results of these tests were sufficiently interesting to raise the question of whether humidity level should also be a variable in these experiments. As a result of those discussions the equipment was further modified to include a solenoid controlled valve to regulate the dry air flow into the dry box. The chamber dehumidification rate in the presence of the dry air flow was carefully characterized to obtain a drying curve for the dry box. This drying curve was integrated into computer-controlled software used for a pulse modulated dehumidification algorithm in which the solenoid valve was opened in a series of predetermined steps to achieve a specific humidity level. The result of these developments was a system whose capability included the ability to run a series of tests on a specific material sample at a variety of voltages under a variety of humidity conditions in a fully automated sequence of tests over the course of many hours (Figure 44).

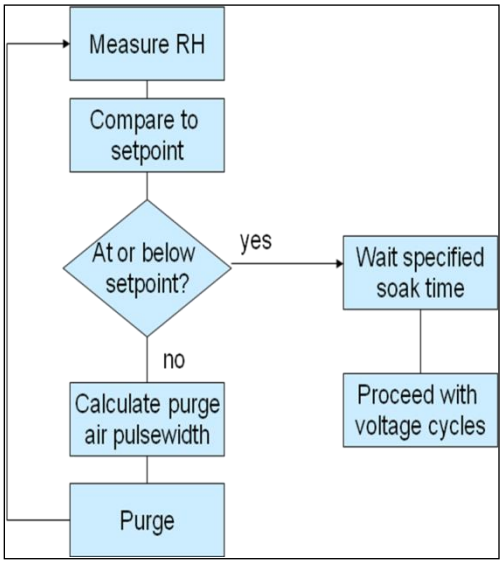

Figure 44. Humidity control algorithm

This research and development initiative enabled the development of laboratory hardware and software for the research into dielectric breakdown characteristics of ostensibly nonconductive battery electrode coatings as a function of both voltage and humidity. It further enabled those tests to be conducted through fully automated test sequences that could take place over several hours with no user input. It facilitated the development of methods and processes that ensured that these measurement technologies were ultimately deployable in a manufacturing environment using typical manufacturing equipment.

4.4.2 Safety testing

Since 2010 ORNL has developed a mechanical “pinch test” to simulate internal short circuit inside a prismatic Li-ion cell. The concept is shown in Figure 45. The main advantage of the pinch test is the ability to create a small short circuit (about 1mm in diameter) deep inside a cell.

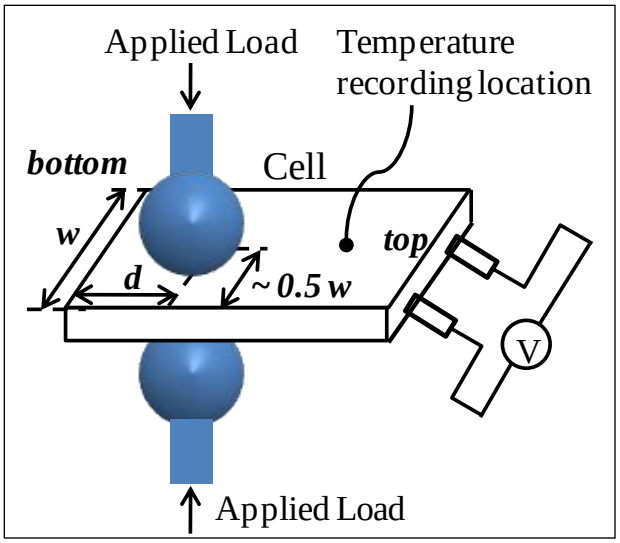

Figure 45. Schematic of the ORNL pinch test.

The mechanical compression was achieved using a servo-hydraulic load system. The system can apply compression to the Li-ion cell at a rate of 15-100 microns/second. The cell voltage is used as the feedback control after a short circuit (voltage drop of 100mV) is detected. By stopping the compression and reducing the applied load quickly, a short circuit can be produced in a single layer. Figure 46 is a typical time vs. displacement and cell voltage plot. The cell response after the short circuit is a good indication of cell safety.

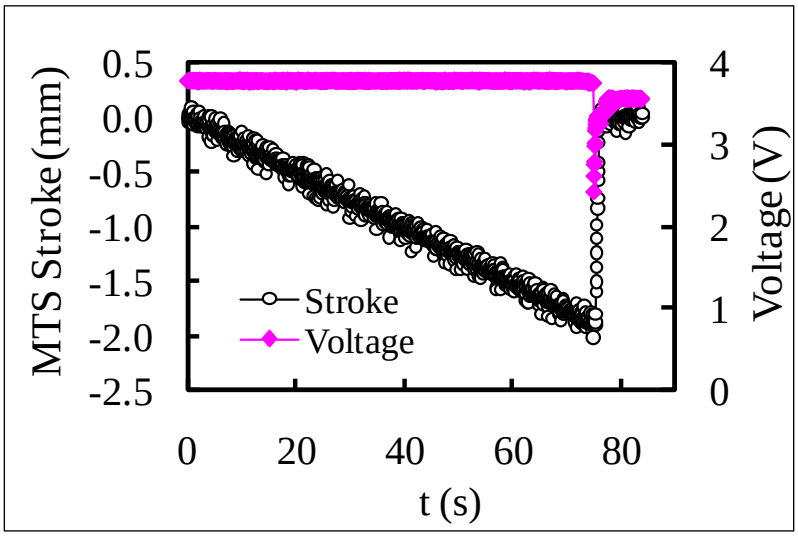

Figure 46. Displacement and Voltage vs. Time plot of a pinch test.

A low-cost system has been designed at ORNL to be more flexible and portable for cell and component testing. The system was built with an electric motor, an actuator and a 2000 pound load cell shown in Figure 47. It has minimum compression speed of 0.0004 mm per second and a voltage feedback loop is used to detect and control the actions after the short circuit. In this design, battery

separators and dry cells can be tested to simulate mechanical deformation in short circuit and crush tests.

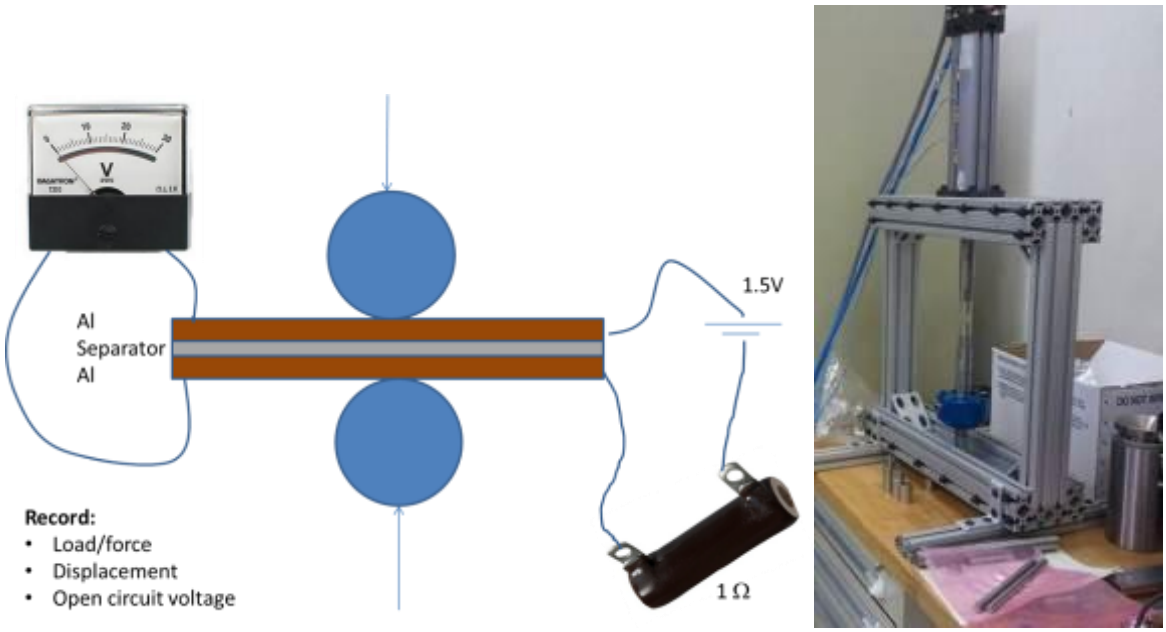

Figure 47. Concept of modified pinch test for cell components and the final setup.

In Figure 48, the typical load and Voltage vs. Time plot showed that the new system can carry out pinch tests similar to nail-pen tests used to evaluate active Li-ion cells. In this particular test, the pinch heads were 25.4 mm diameter brass balls. The separator failed above 200 pounds of load. Upon inspection we found deformation in the brass balls. Another interesting observation was that the separator was compressed to a very thin thickness (from 16 to several microns) without failure. In fact, the pores in the area under compression were completely sealed as shown in Figure 49. In subsequent testing, smaller indenter diameters (<8mm) and the minimum loading speed was used.

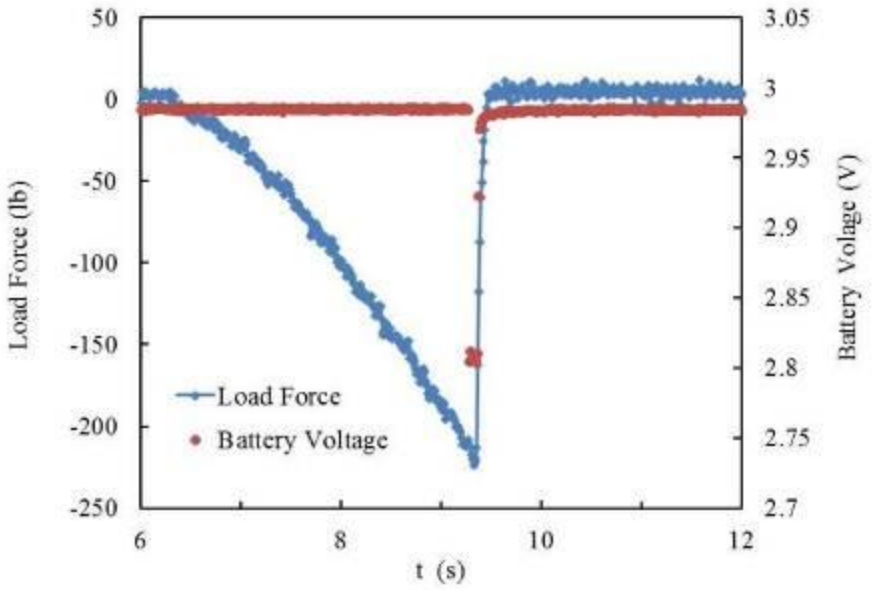

Figure 48. Load and Voltage vs. Time plots during a baseline separator test.

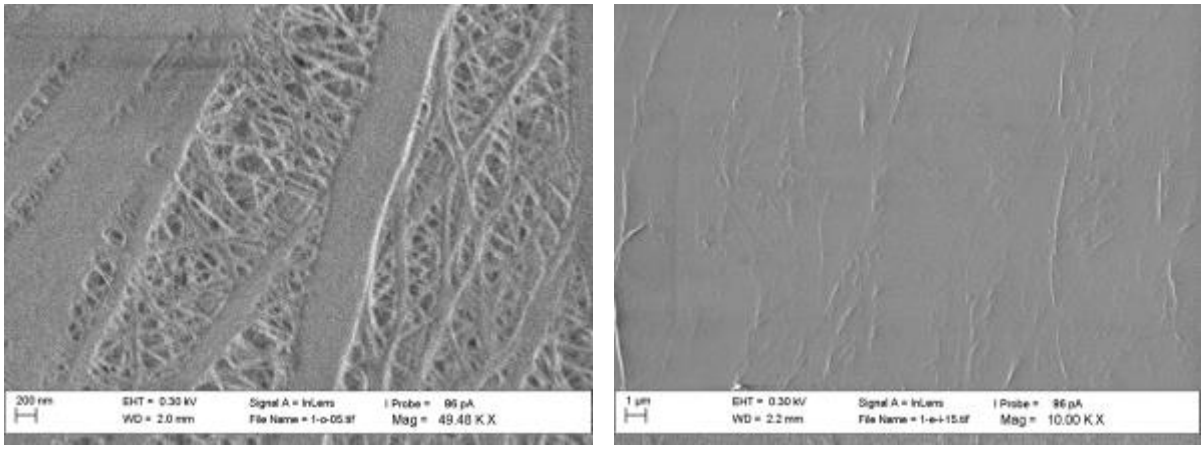

Figure 49. Separator areas with original porosity (left) and area under the compression (right).

Testing of cell components and dry cells

Several types of samples were tested in this project to provide information of the behavior of ceramic coatings under mechanical load. The test matrix was designed using the following combinations:

- Metal - Separator - Metal
- Metal – Ceramic coated separator – Metal
- Anode – Ceramic coated separator – Cathode
- Ceramic coated Anode – Separator – Cathode
- Ceramic coated Anode – Separator – Ceramic coated Cathode
- Anode – Separator – Ceramic coated Cathode

Most of these samples were enclosed in a dry pouch. Pinch test using the same loading parameters

were carried out. As expected, when metal-to-metal contact is initiated due to separator failure, the voltage drop was very sharp, Figure 50. However, when the same test was conducted on current collectors coated with electrode materials on both sides (Figure 51), we observed two interesting behaviors:

The load curve was not a straight line. "Steps" were observed due to the sliding of the layers during very slow loading.

1) Before final breakdown, a noticeable slope change was observed in the voltage and sometimes pre-breakdown events (small voltage drop followed by recovery) would occur.

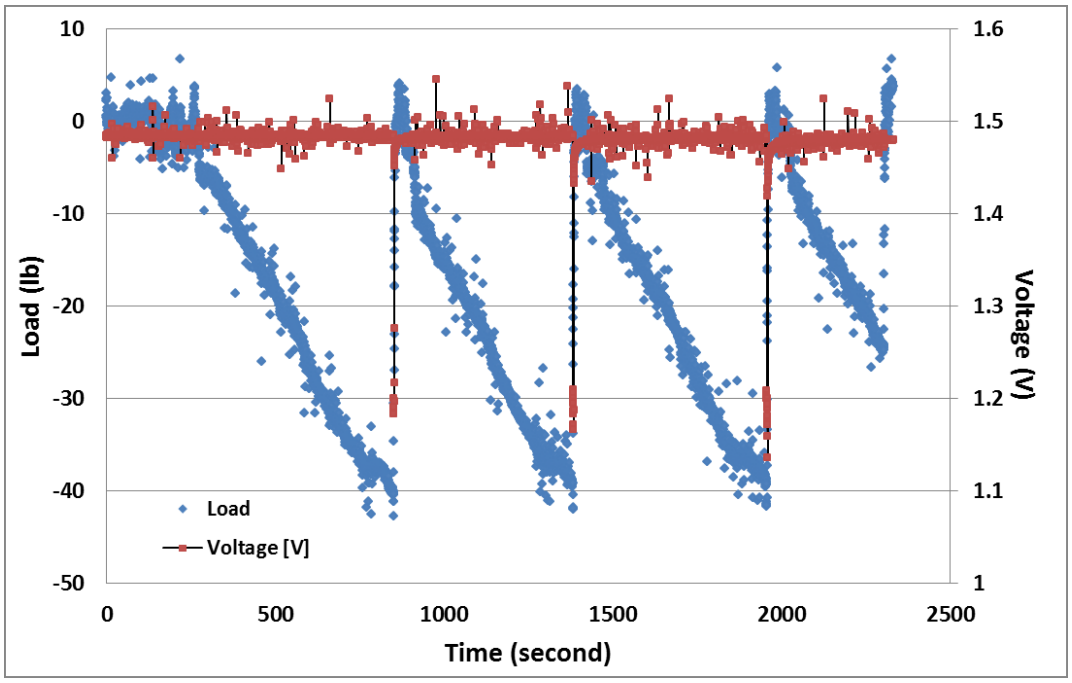

Figure 50. Typical Metal-Separator-Metal sample with sharp voltage drop at failure point.

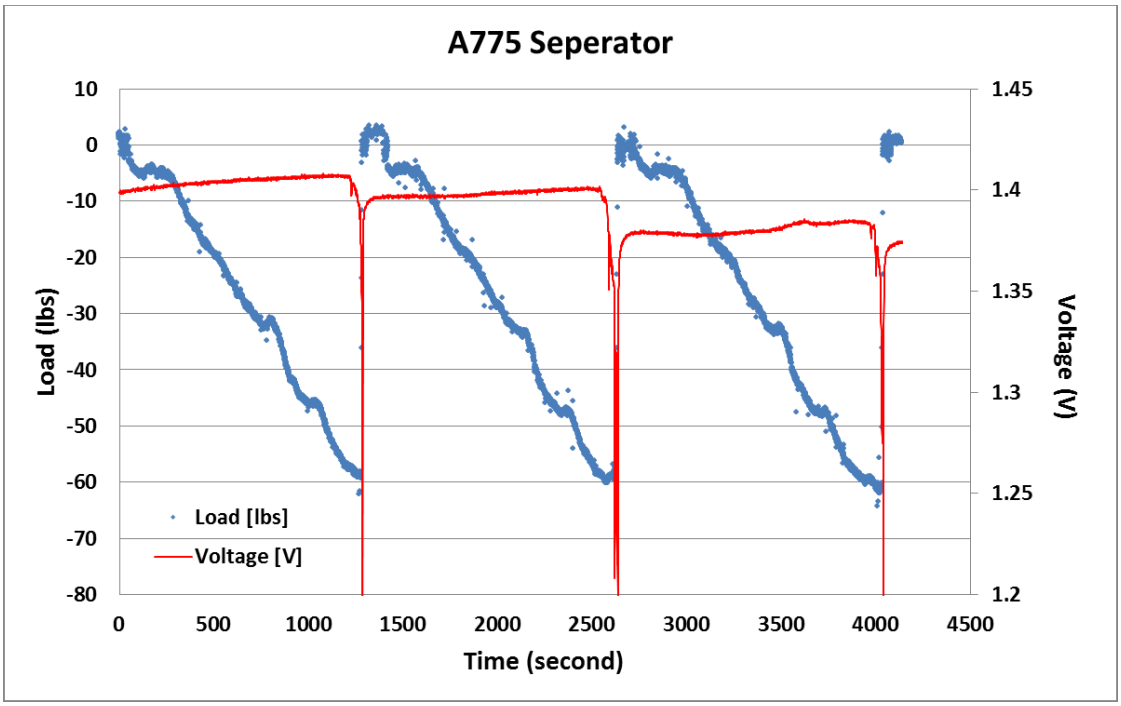

Figure 51. Typical Anode – separator – Cathode sample with sloped voltage drop prior to the failure point.

When the separator is coated with up to a 10 micron thick ceramic coating very similar load "steps" and slope change was observed (Figure 52). At a closer look of the pre-breakdown region, very clear slope changes and pre-breakdown events were observed (Figure 53).

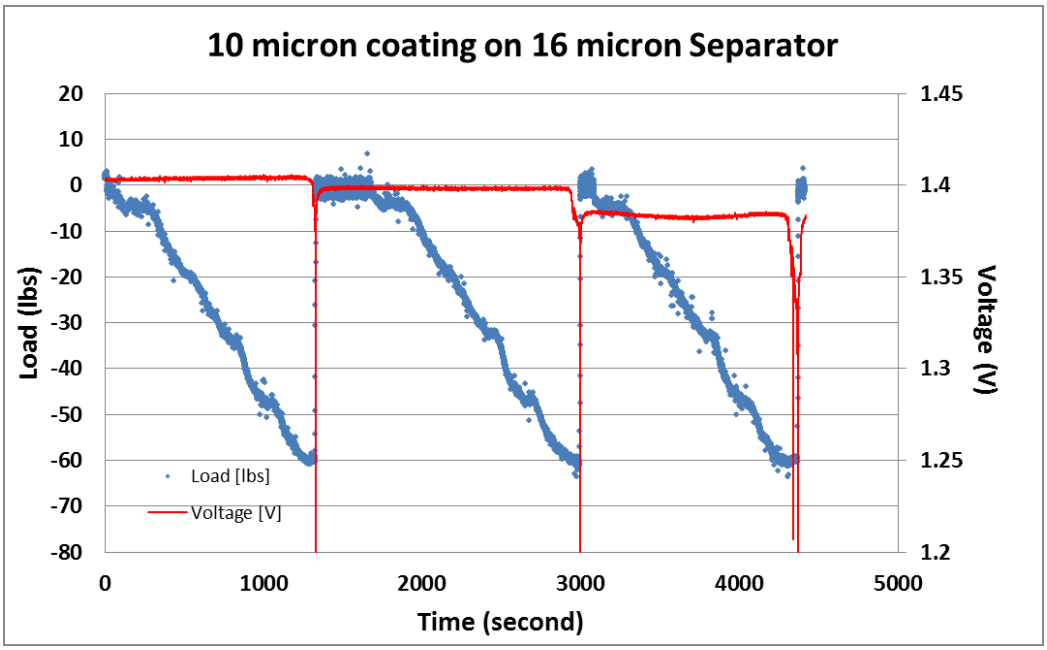

Figure 52. Anode – Ceramic coated separator – Cathode sample with sloped voltage drop prior to the failure point.

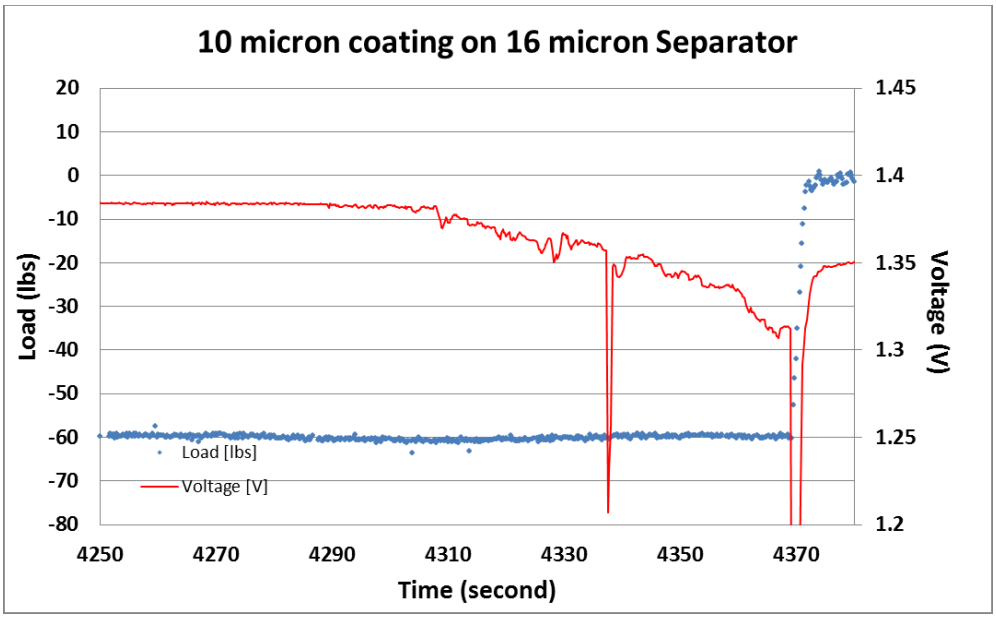

Figure 53. Close-up look at Anode – Ceramic coated separator – Cathode sample with sloped voltage drop prior to the failure point.

Summary

The motor-driven pinch test system developed at ORNL could be used to evaluate the mechanical behavior of cell components under compressive load. The results indicated that the pinch test could reveal the mechanical failure mode of the separator and various dry pouch assemblies. The various electrical contacts gave distinct contact resistance induced voltage vs. time curves. This technique can be used to design basic cell components and evaluate safety related failure behavior.

5. SUBJECT INVENTIONS

Two invention disclosures were filed resulting from the project as outlined below. The process development led to a development of an in-situ system for drying evaluation and an in-line quality control system. Both invention disclosures are under evaluation for patent application.

5.1 IN-SITU DRYING EVALUATION

An apparatus, a method, and a modeling procedure were developed to optimize drying methodology for slurry processing, and film and coating casting. The technology allows for an in-situ observation of drying phenomena and mechanisms and the development of flaws in the coating as they appear. The procedure can optimize the drying methodology for time and flawlessness in coating development and slurry drying. An infrared spot heater is combined with a microscope, a balance, and a thermal probe to dry a slurry and measure mass loss, evaporation rate, shrinkage, and crack or flaw development. Optimization can be tuned based on measurements and understanding resulting from drying simulation and modeling component.

5.2 IN-LINE QUALITY CONTROL PROCEDURE

An apparatus and method for in-line hi-pot testing and selection and elimination of flawed material in electrically or electrochemically important components for applications was developed. The technology allows for an in-situ observation of dielectric and electric parameters as material is fed through or manufactured in a winding or similar procedure. Electrically conductive rolls or a roll and a plate or a roll and a conductive substrate are used as working and counter electrodes. The material of interest is fed through the apparatus as the electrodes are exposed to a set voltage. As a current is detected, the material is determined as flawed and can be marked and eliminated from further manufacturing.

6. COMMERCIALIZATION POSSIBILITIES

Wanxiang/A123 will own the technology but Navitas Systems who purchased the government contract part of A123 Systems in Ann Arbor will have the right to practice it. Navitas will have more opportunities to explore use of this technology as they will be developing a diverse portfolio of cell chemistries mostly for military applications. For example, applications such as the BB-2590 battery for soldier power and combat equipment will require safe operation under a diverse set of conditions. Separators such as NCS could help enable the use of certain cell chemistries for this application.

When NCS is employed for any battery configuration the use of the in-line Hi-Pot flaw detection method described in this report would certainly be a logical addition to the coating line. Much like in polyolefin separator production where optical density variation is used for flaw detection, areas that show leakage current above a certain pre-determined acceptable limit can be flagged for non-use when electrodes are stamped.

Another point to consider is the use of the technology developed here for designing other coating systems. For example, A123 Systems has considered using IR assisted drying for anode and cathode lines but did very little exploratory work in this area to determine whether this could help increase coating rates. As outlined in this report the drying model developed here is directly applicable to understanding and improving IR assisted drying systems design. It certainly is an opportunity worth pursuing.

Another potential application would be to extend the drying model to determine the effect of non-uniform drying on coating quality in commercial systems. The large anode coating system in Romulus, MI uses a drying system where the wet coating is dried in seven different stages. Each of these stages can be maintained at a different temperature dependent on how rapidly the coating is to be dried which in turn depends on the solvent content, electrode loading and coating speed. Some properties, such as adhesion for example, can be negatively impacted by the drying rate especially when a smooth Cu surface is used as the current collector (roughened surfaces of course show much better adhesion because of the ability of the binder to fill the surface pores). The drying model results obtained for different temperature gradients within the drier coupled with adhesion results would be very useful for optimizing this property. Models could also be run for different binder compositions and solids content to examine their effect.

7. PLANS FOR FUTURE COLLABORATION

ORNL has a number of collaboration plans with A123, other battery manufacturers, materials suppliers, and original equipment manufacturers. The collaboration with A123 led to a deeper understanding of NCS and the possible utilization of NCS as a heat resistant layer. We also developed patentable quality control and testing procedures and apparatuses which will be giving opportunities for future collaborations. ORNL's focus is to provide characterization capabilities and processing knowledge to streamline battery manufacturing and reduce cost in the future to meet DOE's cost targets for a variety of applications.

8. CONCLUSIONS

As a result of the collaborative effort between A123 Systems and ORNL to enable the commercial implementation of NCS the following important conclusions were achieved:

1. Temperature variation down and across web along with IR heat fluxes were measured with A123's laboratory scale coater. A large temperature decrease was observed between the end of IR heating and beginning of entrance into the convection oven which could be deleterious to coating quality. In addition, reflectivity and optical and other thermophysical properties were measured as input for the development of new drying models.
2. A radiative model for drying using IR heating was developed and used to simulate the energy transport within semitransparent slurries and coatings. The results indicate that the effect of the NCS coating on the anode was to increase the emissivity from 85% (uncoated anode) to 81% (for coating thickness of 11-75 μm). In addition, less than 2% of the IR energy would be adsorbed in the coating.
3. A mass transfer module was developed for simulating the drying of a porous NCS coating. This enabled the calculation of temperature, fractions of solvent, solids and air and coating height as a function of length along the coated foil for various stages of drying ranging from incomplete drying to complete drying at various distances away from the beginning of IR drying. A specific change in properties was shown to occur at the coherency point, defined as the point where particles come in contact with each other in the partially dried film.
4. A comprehensive model for stress analysis during drying of a coating on flexible substrates was developed. Calculation of mechanical properties of the coating after the coherency point was reached indicate that tensile stresses are likely responsible for the cracking observed in some of the coatings.
5. In addition to understanding the drying of porous media, the coating process was first optimized by insuring slurry quality (e.g., removal of slurry agglomerates and trapped air) and insuring optimal equipment settings (e.g., for coater speed and slot die gap).
6. An online process control method based on dielectic breakdown (Hi-Pot test) for determining coating flaws was developed. This technique has the ability to detect coating defects at production coating speeds.
7. A mechanical pinch test for simulating an internal short circuit was used to evaluate coated electrodes and coated electrode within single layer prismatic cells in dry pouches. Results indicated that this test could be used to evaluate the mechanical failure mode of the separator and dry pouch assemblies.

9. REFERENCES

Alejandro-Arellano, M; Ung, T; Blanco, A; Mulvaney P., and Liz-Marzán, L.M., Silica-coated metals and semiconductors. Stabilization and nanostructuring, Pure and Applied Chemistry, Vol. 72, pp. 257-267, 2000.

Ambrosone, Luigi, Claudio Della Volpe, Gennaro Guarino, Roberto Sartorio, Vincenzo Vitagliano, Free diffusion data in some polymer-solvent systems at 20^{o}C, Journal of Molecular Liquids, Volume 50, Pages 187-196, 1991.

Atakan Avci, Muhiddin Can, The analysis of the drying process on unsteady forced convection in thin films of ink, Applied Thermal Engineering, Volume 19, Issue 6, 1999, Pages 641-657.

Babinec, S., H. Tang, A. Talik, S. Hughes, G. Meyers, Composite cathode structure/property relationships, Journal of Power Sources, 2007, Volume 174, pp. 508-514.

Banerjee B. and Adams D.O, Micromechanics-based determination of effective elastic properties of polymer bonded explosives, Physica B: Condensed Matter, 2003, Vol. 338, pp. 8-15.

Bejan, A., Convection Heat Transfer, 3rd ed., John Wiley and Sons, Inc., Hoboken, NJ (2004).

Biot, M.A., 1941. General theory of three-dimensional consolidation, Journal of Applied Physics, Vol. 12, pp. 155–164.

Bouyer, D., W. Werapun, C. Pochat-Bohatier, A. Deratani, Morphological properties of membranes fabricated by VIPS process using PEI/NMP/water system: SEM analysis and mass transfer modelling, Journal of Membrane Science, Volume 349, Issues 1-2, 1 2010, Pages 97-112.

Brown HR and Yang ACM, 1990, The Propagation of Cracks and Crack-Like Defects in Thin Adhered Polymer-Films, Journal of Materials Science, Vol. 25, pp. 2866-2868.

Chen, Z., Christensen, L. and Dahn, J. R., A study of the mechanical and electrical properties of a polymer/carbon black binder system used in battery electrodes, 2003, Journal of Applied Polymer Science, Vol. 90, pp. 1891–1899.

Design & Processing Guide – Solef^{R} PVDF, Solvay Specialty Polymers, www.SolvaySpecialtyPolymers.com

Di Giuseppe E.; Davaille A.; Mittelstaedt E., and Francois M., Rheological and mechanical properties of silica colloids: from Newtonian liquid to brittle behavior, Rheologica Acta, 2012, Vol. 51, pp. 451-465.

dos Santos, W.N., C.Y. Iguchi, R. Gregorio Jr., Thermal properties of poly(vinilidene fluoride) in the temperature range from 25 to 210 ^{o}C, Polymer Testing, Volume 27, 2008, Pages 204-208

Fedorov A.G. and R. Viskanta, Physics and Chemistry of Glasses 41 (3), 127 (2000).

Gazdaru D.M. and Iorga B., Spectrophotometric Analysis of the Mixtures of Photosynthetic Pigments, Journal of Optoelectronics and Advanced Materials, Vol. 4, 2002, pp. 121 – 129.

Grujicic M, Chittajallu KM, Walsh S, Optimization of the VARTM process for enhancement of the degree of devolatilization of polymerization by-products and solvents, JOURNAL OF MATERIALS SCIENCE, Vol. 38, pp. 3729-3739, 2003.

Hancock BC; York P, and Rowe RC, An Assessment of Substrate-Binder Interactions In Model Granule Systems .3. Linear Elastic Fracture-Mechanics, Journal of Materials Science, 1993, Vol. 28, pp. 6729-6736.

Hellinckx S and Bauwens JC, The yield behavior of PVDF and the deformation process at high-temperature, Colloid and Polymer Science, 1995, Vol. 273, pp. 219-226.

Heslin, T. M., "An equation that describes material outgassing for contamination modeling," 1977, Report NASA-TN-D-8471.

Hsueh, C.H. "Modeling of elastic deformation of multilayers due to residual stresses and external bending," *J. Appl. Phys.* Vol. 91 (2002), pp. 9652-9656.

Iguchi, C.Y., W.N. dos Santos, R. Gregorio Jr., Determination of thermal properties of pyroelectric polymers, copolymers and blends by the laser flash technique, Polymer Testing, Vol. 26, 2007, pp. 788-792.

Jaturonglumlert S. and Kiatsiriroat T., Heat and mass transfer in combined convective and far-infrared drying of fruit leather, Journal of Food Engineering, Vol. 100, 2010, pp. 254-260.

Kaczmarek M. and Marc G., Dependence of elastic properties of materials on their porosity: Review of models, 2006, JOURNAL OF POROUS MEDIA, Vol. 9, pp. 335-355.

Kneisl P, Zondlo Jw, Vapor-Pressure, Liquid Density, And The Latent-Heat Of Vaporization As Functions Of Temperature For 4 Dipolar Aprotic-Solvents, Journal Of Chemical And Engineering Data, Vol. 32, pp. 11-13, 1987.

Levinson, Ronnen, Paul Berdahl, and Hashem Akbari, Solar Energy Materials and Solar Cells 89 (4), 319 (2005).

Maleki, H; Al Hallaj, S; Selman, JR; Dinwiddie, RB; Wang, H, Thermal properties of lithium-ion battery and components, Journal of the Electrochemical Society, Vol. 146, pp. 947-954, 1999.

McCartney L.N. and Kelly A., Maxwell's far-field methodology applied to the prediction of properties of multi-phase isotropic particulate composites, Proc. R. Soc. A, 2008 464, 423-446.

Performance Characteristics & Data for Kynar^{R} and Kynar^{R} Flex PVDF, Atofina, www.kynar.com, www.ATOFINAChemicals.com

Puyate, Y.T. and C.J. Lawrence, Models for predicting drying stresses and strains in a film cast on a substrate: An alternative approach, Chemical Engineering Science, 2009, Vol. 64, pp. 1820-1831.

Rice J.R. and M.P. Cleary, Rev. Geophys. Space Phys. 14 (1976) p.227.

Routh, A.F. and Russel, W.B.A process model for latex film formation: Limiting regimes for individual driving forces, Langmuir, 1999, 15 (22), 7762-7773.

Sabau, A.S., C.I. Contescu, G.D. Jellison, J. Y. Howe, B.L. Armstrong, C. Daniel, P. Hagans, and S. Babinec, Evaporation rates of N-methylpyrrolidinone exposed to infrared heating under natural convection regime, submitted for publication in Journal of Applied Physics, Nov. 5, 2012.

Scherer, G.W., 1986. Drying gels I: general theory. Journal of Non-Crystalline Solids 87, 199–225.

Scherer, G.W., 1989. Drying gels VIII: revision and review. Journal of Non-Crystalline Solids 109, 171–182.

Scherer, G.W., 1990, Theory of drying, Journal of the American Ceramic Society 73, 3–14.

Scherer, G.W., 1990, Stress and Fracture during Drying of Gels, Journal of Non-Crystalline Solids, Vol. 121, 104–109.

Scherer, G.W., 1992a, Crack-tip Stress in Gels, Journal of Non-Crystalline Solids, Vol. 144, 210-216.

Shui H., Wang Z., and Gao J. Examination of the role of CS_2 in the CS_2/NMP mixed solvents to coal extraction, 2006, Fuel Processing Technology, Vol. 87, pp. 185-190.

Siegel R. and J. R. Howell, Thermal Radiation Heat Transfer. (Taylor and Francis-Hemisphere, Washington, 2001).

Stoney, G.G. Proc. R. Soc. London, Ser. A, Vol. 82, p. 172, 1909.

Suvorov A.P. and A.P.S. Selvadurai, Macroscopic constitutive equations of thermo-poroelasticity derived using eigenstrain–eigenstress approaches, Philosophical Magazine, Vol. 91, pp. 2317-2342.

Tirumkudulu, M.S. and Russel, W.B., Role of capillary stresses in film formation, Langmuir, 2004, 20, pp. 2947-2961.

Tirumkudulu, M. Russel, W. B. Cracking in drying latex films. Langmuir, 2005, Vol. 21, pp. 4938-4948.

Tsay C.S. and McHugh A.J., Mass transfer dynamics of the evaporation step in membrane formation by phase inversion, Journal of membrane science, 1991, Vol. 64, pp. 81

Wang, J. C., Young's modulus of porous materials, J. Mater. Sci., vol. 19, pp. 801–808, 1984.

Yanagida T; Matchett AJ; Coulthard JM, Asmar, B.N., Langston, P.A., Walters, J.K., Dynamic measurement for the stiffness of loosely packed powder beds, AICHE JOURNAL, 2002 Vol. 48, pp. 2510-2517.

Yip, Y. and A.J. McHugh, Modeling and simulation of nonsolvent vapor-induced phase separation, Journal of Membrane Science, Volume 271, 2006, Pages 163-176.

Zarzycki J, 1988, Critical stress intensity factors of wet gels, J Non-Cryst Solids Vol. 100, pp. 359–363.